Secondary flows in turbulent boundary layers over longitudinal surface roughness

Hyeon Gyu Hwang and Jae Hwa Lee*
School of Mechanical, Aerospace and Nuclear Engineering, UNIST, 50 UNIST-gil, Eonyang-eup, Ulsan 44919, Korea

(Received 29 August 2017; published 18 January 2018)

Direct numerical simulations of turbulent boundary layers over longitudinal surface roughness are performed to investigate the impact of the surface roughness on the mean flow characteristics related to counter-rotating large-scale secondary flows. By systematically changing the two parameters of the pitch (P) and width (S) for roughness elements in the ranges of $0.57 \leqslant P/\delta \leqslant 2.39$ and $0.15 \leqslant S/\delta \leqslant 1.12$, where δ is the boundary layer thickness, we find that the size of the secondary flow in each case is mostly determined by the value of $P-S$, i.e., the valley width, over the ridge-type roughness. However, the strength of the secondary flows on the cross-stream plane relative to the flow is increased when the value of P increases or when the value of S decreases. In addition to the secondary flows, additional tertiary and quaternary flows are observed both above the roughness crest and in the valley as the values of P and S increase further. Based on an analysis using the turbulent kinetic energy transport equation, it is shown that the secondary flow over the ridge-type roughness is both driven and sustained by the anisotropy of turbulence, consistent with previous observations of a turbulent boundary layer over strip-type roughness [Anderson *et al.*, J. Fluid Mech. **768**, 316 (2015)]. Careful inspection of the turbulent kinetic energy budget reveals that the opposite rotational sense of the secondary flow between the ridge- and strip-type roughness elements is primarily attributed to the local imbalance of energy budget created by the strong turbulent transport term over the ridge-type roughness. The active transport of the kinetic energy over the ridge-type roughness is closely associated with the upward deflection of spanwise motions in the valley, mostly due to the roughness edge.

DOI: 10.1103/PhysRevFluids.3.014608

I. INTRODUCTION

Streamwise flow circulation or swirling motion normal to the primary flow, commonly called a "secondary flow," is one of the most widely observed flow phenomena. When a secondary flow is superimposed on a primary flow, the flow is characterized by helical motion about the streamwise axis, leading to a significant enhancement of flow mixing throughout the entire boundary layer. From the early history of fluid dynamics, the underlying physics of secondary flows in numerous flow types have been studied because these factors have a strong impact on the main flow, even with a relatively small magnitude of circulating motion. Nikuradse [1] was the first to observe a mean secondary flow motion and related streamwise mean velocity distribution in an experiment on a turbulent duct flow with a non-circular cross-section. Prandtl [2] suggested a comprehensive classification of secondary flows depending on the generation mechanism: the first kind of secondary flow is created by a pressure gradient or centrifugal force, which results from the curvature of the flow path, and the second kind of secondary flow is generated by the anisotropy of turbulence. In

*jhlee06@unist.ac.kr

contrast to the first kind, which can occur in either a laminar or a turbulent flow through an inviscid generation mechanism, secondary flows of the second kind necessitate the presence of turbulence by definition. With regard to the second kind of secondary flow, Hinze [3,4] and Perkins [5] suggested formation mechanism of secondary flow in turbulent flows using turbulent kinetic energy (tke) and mean streamwise vorticity transport equations.

Significant efforts have been devoted to reveal the characteristics of secondary flows in turbulent flows with spanwise heterogeneous surface conditions [6–10]. In an experimental study of turbulent open channel flows with strip- and ridge-type roughness, Wang & Cheng [10] showed secondary flows are generated over spanwise heterogeneous surface condition for both types of roughness. In their experiment, strip- and ridge-type roughness were distinguished based on the roughness height over an elevated (high-drag) region; e.g., a small elevation compared to a recessed (low-drag) region denoted strip-type roughness and a large elevation was ridge-type roughness. They found that the rotational sense of the generated secondary flow is affected by the roughness type. In addition, Willingham *et al.* [6] performed large-eddy simulations (LESs) of turbulent boundary layers (TBLs) over spanwise-alternating high and low roughness virtually reproduced by the spanwise variation of wall shear stress imposed over a flat plate (e.g., strip-type roughness). When the spacing between the elements with high roughness elements was fixed, decreasing the width of the high roughness (or increasing the height ratio between high- and low-roughness) increased the imposed wall stresses on the high-roughness significantly, resulting in an enhancement of the transverse mixing. Recently, an experimental study by Vanderwel & Ganapathisubramani [9] of a TBL over ridge-type longitudinal roughness elements examined the effects of the size and strength of a secondary flow when the spanwise spacing between the roughness elements was varied but with fixed roughness widths and heights. Although the secondary flow was confined in the vicinity of the roughness for a small spacing, the size and strength of the secondary flow were increased with an increase of the spacing until the roughness spacing was comparable to the boundary layer thickness. In addition, as the spacing increased beyond the boundary layer thickness, a tertiary flow was formed in the valley, whose size and strength were smaller than that of the existing secondary flow.

Furthermore, Barros & Christensen [7] and Mejia-Alvarez & Christensen [8] investigated the spatial relevance of secondary flows with regard to spanwise heterogeneity of the mean flow and turbulent Reynolds stresses. In a TBL on a replica of a damaged turbine blade, which featured multiscale complex roughness, they showed that the ensemble-averaged streamwise velocity has spanwise heterogeneity in the form of a spanwise-alternating "low momentum pathway" (LMP) and "high momentum pathway" (HMP). These localized momentum pathways were consistently flanked by the streamwise counter-rotating circulation of a secondary flow. In those studies, the secondary flow exhibited wall-normal diverging motion (a positive wall-normal velocity) in the region of the LMPs, by which the low momentum from the wall was transported toward the outer region. In contrast, converging motion (a negative wall-normal velocity) was observed at the regions of HMPs, leading to the convection of higher momentum toward the wall. In regions of LMPs, the turbulent kinetic energy and Reynolds shear stress were dramatically enhanced. Following work by Willingham *et al.* [6], a LES study by Anderson *et al.* [11] reported that the downward motion of secondary flows in HMP regions is created by the realization of the advective velocity of tke, which is necessary for global energy conservation. This result indicated that the emergence of a secondary flow in a TBL with spanwise heterogeneous surface condition is due to Prandtl's second kind.

Although LMPs (or HMPs) are closely associated with upward (or downward) motion regardless of a strip- or ridge-type roughness element in a turbulent flow [6,9,12], a careful review of previous studies suggests that spanwise locations for LMPs and HMPs and the associated rotational sense of the secondary flow are significantly influenced by the type of roughness. For the strip-type roughness, the formation of HMPs with converging motion was observed in regions of higher drag [6–8,10–12]. However, for the ridge type of roughness, HMPs with downward motion were found in region with lower drag regions (e.g., recessed regions). For the rotational directions and associated spanwise locations of LMPs and HMPs, Willingham *et al.* [6] argued that because a region with locally higher drag pulls the momentum toward the wall, local thinning of the boundary layer with a HMP is

created at the region with a higher drag region. For instances of ridge-type roughness, Vanderwel & Ganapathisubramani [9] and Wang & Cheng [10] suggested that the occurrence of HMPs in recessed regions is induced because higher momentum is more easily observed in recessed regions due to the absence or the reduced blockage effect of the main flow. Thus, the dynamics of secondary flow formation and the spatial features of mean flows over ridge-type roughness may differ from those over strip-type roughness.

It is worth mentioning previous research on the dynamics of secondary flows in turbulent flows induced by spanwise heterogeneous surface conditions. An experimental study by Vermaas *et al.* [13] investigated the streamwise developing spanwise momentum exchange process over a longitudinal surface composed of smooth and rough (strip-type) walls. In the initial stage of a rough wall, spanwise motions associated with mixing from a decelerating flow over the rough wall to an accelerating flow over the smooth wall were mainly caused by the mass transfer. However, as the flow moved downstream, the amount of mass transfer decreased due to the adaptation of the flow to the surface conditions, while lateral momentum transfers were sustained by secondary flows. In a turbulent flow over a super-hydrophobic surface (SHS), it was reported that spanwise variation of the wall shear stress, consisting of regions of high and low drag with a no-slip surface and a shear-free surface, generates a secondary flow [14,15]. Although downward motion was observed over the no-slip region with a large width of the no-slip region, the sense of rotation of the secondary flow over the no-slip region was reversed for a small width. Stroh *et al.* [14] and Türk *et al.* [15] attributed the change of the rotational sense of the secondary flow to the formation of a tertiary flow with a rotational direction opposite to that of the existing secondary flow. For a turbulent flow with riblets, Goldstein & Tuan [16] performed a numerical experiment to provide an alternative way of explaining the formation of a secondary flow. They applied only a spanwise no-slip condition on a single fin (riblet) and showed that the damping of spanwise motion at the side wall of the fin plays an important role in generating a secondary flow by deflecting the cross-flow near the wall in an upward direction. The importance of cross-flow deflection during the formation of a secondary flow over ridge-type roughness was also reported in Wang & Cheng [10].

In the present study, direct numerical simulations (DNSs) of TBLs over longitudinal surface roughness are conducted to investigate the impact of the surface roughness on the mean flow characteristics related to secondary flows. In particular, a special focus is on the origin of the distinctive rotational sense of the secondary flow depending on the type of roughness elements, e.g., ridge- and/or strip-type roughness. To impose ridge-type roughness with an abrupt spanwise transition of the roughness elevation in the flow, longitudinal roughness elements with a height (H) of $H/\theta_{in} = 1.5$ are periodically arranged in the spanwise direction while varying the two parameters of the spacing (P) and roughness width (S) in the corresponding ranges of $12 \leqslant P/\theta_{in} \leqslant 48$ and $3 \leqslant S/\theta_{in} \leqslant 24$, where θ_{in} is the inlet momentum thickness. The range of the Reynolds numbers used is $\mathrm{Re}_\theta = 300 \sim 900$. We examine the spatial development of a secondary flow to clarify how the secondary flow is created along the streamwise direction after a step change from a smooth wall to a rough wall. Furthermore, the spatial characteristics of the sizes and strengths of secondary flows in equilibrium are investigated to identify the important parameters determining the characteristics of TBLs over ridge-type roughness. Finally, the energy budget terms in the tke transport equation are analyzed to reveal the formation mechanism of secondary flows in TBLs over longitudinal surface roughness, and the results are compared with previous findings pertaining to strip-type roughness elements to examine the origin of the opposite sense of rotation between the ridge- and strip-type roughness elements.

II. NUMERICAL METHOD

For an incompressible flow, the nondimensional governing equations are

$$\frac{\partial u_i}{\partial t} + \frac{\partial u_i u_j}{\partial x_j} = -\frac{\partial p}{\partial x_i} + \frac{1}{\mathrm{Re}} \frac{\partial^2 u_i}{\partial x_j \partial x_j} + f_i \quad \text{and} \tag{1}$$

$$\frac{\partial u_i}{\partial x_i} = 0, \tag{2}$$

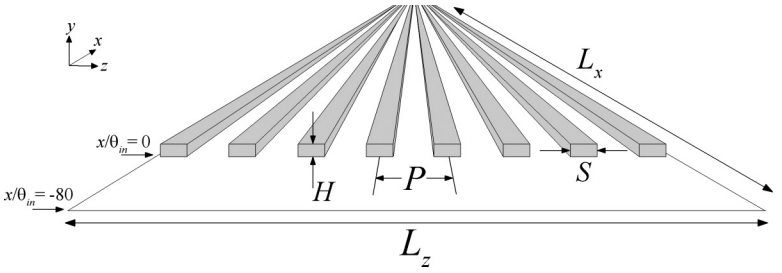

FIG. 1. Schematic of a turbulent boundary layer with longitudinal surface roughness. Roughness elements with height H and width S are periodically arranged in the spanwise direction with pitch P. A step change from a smooth to a rough surface occurs at $80\theta_{in}$ downstream from the inlet, which is defined as $x/\theta_{in} = 0$.

where x_i denotes the Cartesian coordinates and u_i represents the corresponding velocity components. All variables are nondimensionalized by the free-stream velocity (U_∞) and the momentum thickness at the inlet (θ_{in}). The Reynolds number is defined as $\mathrm{Re}_\theta = U_\infty\theta/\nu$, where ν is the kinematic viscosity. All terms are resolved with the Crank-Nicolson method in time and by the central difference scheme in space with a staggered mesh. The equations are integrated over time using the fractional step method along with the implicit velocity decoupling procedure [17]. Block LU decomposition based on approximate factorization is applied to achieve both velocity-pressure decoupling and additional decoupling of the intermediate velocity components. In this approach, decoupled velocity components are solved without iteration, reducing the computation time significantly. The immersed boundary method using discrete forcing is used to describe longitudinal roughness elements with Cartesian coordinates and a rectangular domain [18]. For the discrete forcing method, the desired value of the velocity is directly imposed on the boundary without any dynamical process and is calculated from the velocity components, which is explicitly updated from the previous time step. The desired velocity is estimated based on nearby forcing point through the appropriate second-order linear and bilinear interpolations.

A schematic of a TBL over the longitudinal surface roughness is shown in Fig. 1. The notation adopted is such that x, y and z denote the streamwise, wall-normal and spanwise coordinates, respectively, while u, v and w denote the corresponding streamwise, wall-normal and spanwise velocity components. The longitudinal roughness elements of the pitch (P) and width (S) are periodically arranged in the spanwise direction with a fixed height of H. In the present study, nine simulations in total for rough-wall TBLs with varying P and S values are conducted to examine the effects of the parameters on secondary flows and the TBL flow over a smooth wall is calculated for comparison. The corresponding domain sizes and mesh resolutions are summarized in Table I. The simulation names in the first column in Table I indicate the pitch spacing (P) between the

TABLE I. Computational details for the simulations.

	$\mathrm{Re}_{\theta in}$	N_x, N_y, N_z	$L_x/\theta_{in}, L_y/\theta_{in}, L_z/\theta_{in}$	Δx^+	$\Delta y^+{}_{\mathrm{min}}$	Δz^+	$\Delta t U_\infty/\theta_{in}$
Smooth	300	2049, 150, 513	768, 60, 96	6.0	0.2	3.0	0.3
*P*12*S*3	300	2049, 150, 513	768, 60, 96	6.0	0.2	3.0	0.3
*P*12*S*6	300	2049, 150, 513	768, 60, 96	6.0	0.2	3.0	0.3
*P*24*S*3	300	2049, 150, 513	768, 60, 96	6.0	0.2	3.0	0.3
*P*24*S*6	300	2049, 150, 513	768, 60, 96	6.0	0.2	3.0	0.3
*P*24*S*12	300	2049, 150, 513	768, 60, 96	6.0	0.2	3.0	0.3
*P*48*S*3	300	2049, 150, 513	768, 60, 96	6.0	0.2	3.0	0.3
*P*48*S*6	300	2049, 150, 513	768, 60, 96	6.0	0.2	3.0	0.3
*P*48*S*12	300	2049, 150, 513	768, 60, 96	6.0	0.2	3.0	0.3
*P*48*S*24	300	2049, 150, 513	768, 60, 96	6.0	0.2	3.0	0.3

longitudinal surface roughness and the roughness width (S); for example, $P12S3$ denotes the case of a TBL flow with longitudinal roughness with $P/\theta_{in} = 12$ and $S/\theta_{in} = 3$. The values of P and the width S are selected to cover a wide range of roughness spacings ($0.57 \leqslant P/\delta \leqslant 2.39$) and widths ($0.15 \leqslant S/\delta \leqslant 1.12$) in a state of equilibrium. Although not shown here, a grid sensitivity study with doubled streamwise and spanwise resolutions for computational feasibility indicated that the influence of mesh resolution is negligible since difference in the maximum value of the wall shear stress between the present resolution and the doubled resolution is less than 2%. The domain size employed here is confirmed to be adequate based on the convergence of the two-point correlations to zero for half of the present domain in the streamwise and spanwise directions. In addition, direct comparison of DNS data between the current domain and doubled spanwise domain size suggests that there is little influence on the computational domain size for investigating the spatial characteristics of secondary flows. A non-uniform grid distribution is employed in the wall-normal direction using a hyperbolic tangent function, and uniform grid distributions are used in both the streamwise and spanwise directions. A no-slip boundary condition is imposed at the solid wall and the free-stream velocity ($u = U_\infty$) and shear free conditions ($\partial v/\partial y = \partial w/\partial y = 0$) are specified as boundary conditions on the top surface of the computational domain. A periodic boundary condition is applied in the spanwise direction. Because the boundary layer develops spatially in the downstream direction, an auxiliary simulation is carried out to acquire time-dependent inflow data ($\mathrm{Re}_\theta = 300$) for the inlet boundary condition [19]. Although not shown here, turbulence statistics were compared with the DNS data of Spalart [20] at $\mathrm{Re}_\theta = 300$ to ascertain the reliability and the accuracy of the inflow data [21]. At the domain exit, a convective boundary condition is used, as $(\partial u/\partial t) + c(\partial u/\partial x) = 0$, where c is the local bulk velocity. To avoid generating a rough wall inflow, the longitudinal roughness elements are placed at the position of $80\theta_{in}$ downstream from the inlet (Fig. 1); thus, the surface condition changes abruptly from a smooth to a rough wall at this location, which is defined as $x/\theta_{in} = 0$.

To determine the turbulent statistics over the spanwise heterogeneous surface roughness, a phase-averaging technique is employed with temporal averaging in the present study. The phase- and temporal-averaged mean quantities are denoted by brackets, $\langle\,\rangle$, and the velocity fluctuations (u_i') are defined from the phase-averaged values: $u_i' = u_i - \langle u_i \rangle$. In addition, spatial averaging of $\langle u_i \rangle$ in the spanwise direction is adopted to estimate the spatial mean (e.g., $\langle u_i \rangle_z$). Capital letters indicate temporal and spatially averaged statistics (e.g., $U_i = \langle u_i \rangle_z$), and the superscript $+$ indicates the quantities normalized by the friction velocity (U_τ). The sampling time duration was $60\,000\theta_{in}/U_\infty$, which is sufficient to allow particles to travel more than 50 times through the streamwise dimension at the bulk velocity.

III. RESULTS AND DISCUSSION

A. Self-preservation of the rough wall turbulent boundary layer

Because a TBL flow spatially develops in the streamwise direction with a step change from a smooth to a rough wall, it is important to consider where a new equilibrium state with a self-preserving form is established. Perry *et al.* [22] and Smalley *et al.* [23] suggested conditions for self-preservation in a rough wall TBL that the boundary layer thickness should increase linearly along the streamwise direction and that the friction velocity should be mostly constant along the streamwise direction. To determine self-preservation in a rough wall TBL, the spatially averaged skin-frictional drag (C_f), form drag (P_d) and friction velocity normalized by the free-stream velocity (U_τ/U_∞) with an increase of P are shown in Fig. 2 with a fixed value of S. The data of a smooth wall is included for comparison. In Fig. 2(a), the values of C_f over the rough walls are larger than those of the smooth wall due to an increase in the surface area caused by the introduction of roughness elements. In particular, an inspection of the spanwise variation of wall shear stress reveals that most of the increase in the wall shear stress occurs at the side walls and roughness edge (not shown here). As the value of P decreases, the values of C_f increase due to the larger number of roughness elements with a decrease of P. In Fig. 2(b), the value of P_d over the longitudinal surface roughness is nearly zero along the streamwise direction, except for a region near the roughness step change. The normalized friction velocity

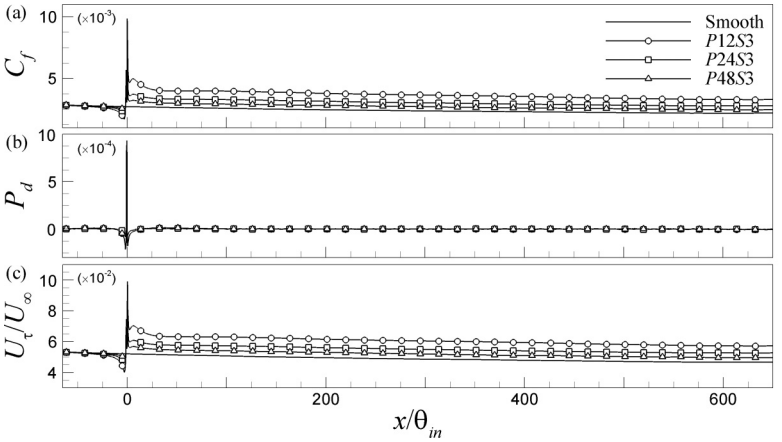

FIG. 2. Variations of the spanwise-averaged (a) skin-friction drag (C_f), (b) form the drag (P_d) and (c) friction velocity (U_τ/U_∞) along the downstream direction.

(U_τ/U_∞) in Fig. 2(c) exhibits a trend similar to that of C_f with an increase in P, as the contribution to the total drag is completely from C_f under the present roughness configuration. The values of U_τ/U_∞ for all P converge to the range of $0.050 \sim 0.062$ for conditions in which $x/\theta_{in} > 220$. These values of U_τ/U_∞ are much smaller than those of TBL flows with a transverse rod [24] and cube [21] despite the fact that the roughness heights are identical ($H/\theta_{in} = 1.5$). Although the width of the surface roughness in Fig. 2 is fixed at $S/\theta_{in} = 3$, the overall trend of the statistics is not affected by an increase of S (not shown here).

Figure 3 shows the streamwise variation of the boundary layer thickness (δ/θ_{in}), displacement thickness (δ^*/θ_{in}), momentum thickness (θ/θ_{in}) and shape parameter (H) as the value of P is varied. In Fig. 3(a), δ increases almost linearly along the streamwise direction after the roughness step change. Although there is slight downward shift of δ with an increase of x/θ_{in}, δ is less sensitive to variations of P and S. Compared to the variation of δ, δ^* in Fig. 3(b) displays higher values for

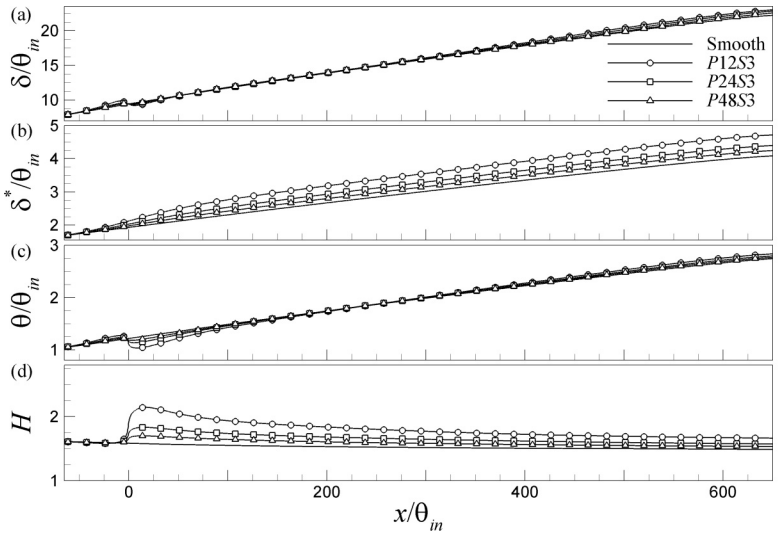

FIG. 3. Variations of the spanwise-averaged (a) boundary layer thickness (δ/θ_{in}), (b) displacement thickness (δ^*/θ_{in}), (c) momentum thickness (θ/θ_{in}) and (d) shape parameter (H) along the downstream direction.

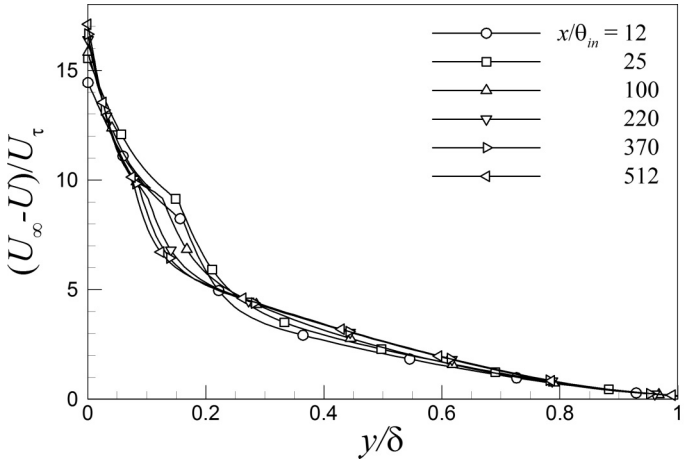

FIG. 4. Variations of the spanwise-averaged mean velocity defect profiles along the downstream direction for $P12S3$.

the rough walls than that over the smooth wall due to the large mean velocity loss caused by the roughness element. In addition, as the value of P increases, the rate of increase for δ^* is lowered due to the presence of a wide valley. On the other hand, the effect of P is negligible on the variation of θ in Fig. 3(c), because the large velocity defect is compensated with a large velocity gradient. In Fig. 3(d), the shape factor, $H(=\delta^*/\theta)$, which provides a useful means of characterizing the state of the development of the boundary layer, increases significantly near the roughness step change owing to flow separation and gradually converges with an increase of x/θ_{in}.

In addition to the boundary layer parameters, the establishment of self-preservation in TBL flows over the surface roughness is examined using profiles of the spanwise-averaged mean velocity defect and Reynolds stresses. Figure 4 shows the streamwise variation of the mean velocity defect profiles for $P12S3$ in the outer coordinates. The profiles become well collapsed at approximately $x/\theta_{in} > 220$. Furthermore, the profiles of the Reynolds stresses along the streamwise direction for $P12S3$ in Fig. 5 exhibit good agreement in the outer layer ($y/\delta > 0.4$) after $x/\theta_{in} = 220$, suggesting the establishment of a self-preservation form. In Fig. 5(a), although the peak values of the streamwise Reynolds normal stress near the step change ($x/\theta_{in} \leqslant 50$) are found to be far from the wall, those in the equilibrium state ($x/\theta_{in} > 220$) are observed slightly above the roughness height ($H/\delta = 0.07 \sim 0.09$) regardless of the streamwise location due to large disturbance effect of the roughness edge on the upcoming main flow. Near the step change, strong impingement of the flow to the roughness, creating three-dimensional random disturbances, contributes to the generation of a large amount of turbulent energy in the outer layer. As the flow moves along the downstream direction, the wall-normal locations become closer to the wall for the peaks of the Reynolds stresses due to the increase of the boundary layer thickness. In addition, the increase of the near-wall peaks for the Reynolds normal and shear stresses when moving downstream is induced by the decrease of the friction velocity (and most likely the Reynolds number effect).

Although the self-preservation of the TBL over the roughness for $P12S3$ is shown to be achieved at approximately $x/\theta_{in} > 220$ based on the boundary layer parameters (Figs. 2 and 3) and turbulent statistics (Figs. 4 and 5), a closer analysis of the statistics with respect to the values of P and S in Fig. 6 suggests that the streamwise location for the establishment of the self-preservation of TBL flows over the surface roughness is significantly affected by the value of P. Here, the equilibrium locations (x_{eq}) for all P and S are estimated using a procedure identical to that of $P12S3$ above. Because the longitudinal surface with a large value of P is characterized by significant spanwise heterogeneity of surface condition, resulting in strong random disturbances emanating from the interaction between the near-wall structures and the roughness, the transitional effects of the step change persist for an

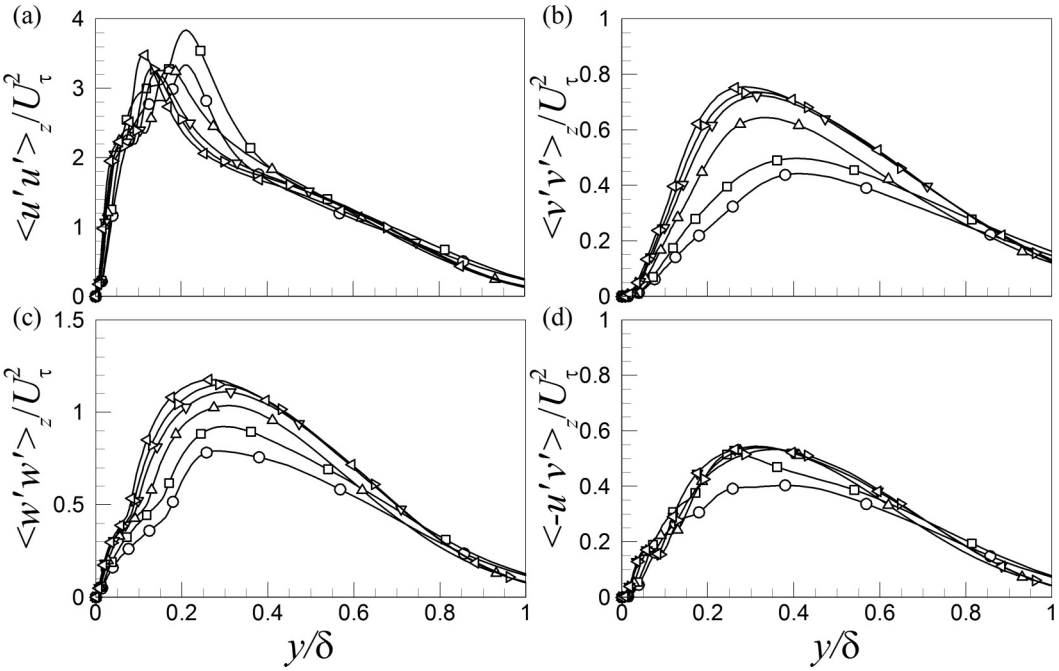

FIG. 5. Variation of the turbulent Reynolds stresses along the streamwise direction for $P12S3$. The line symbols are identical to those in Fig. 4.

extended period in the downstream direction with an increase of P. The little influence of the value of S on the streamwise distance required to achieve a state of equilibrium at a fixed value of P is expected, as the number of roughness edges, which is important to characterize the flow, is identical at a fixed value of P, while the value of S is varied. Compared to previous findings ($x_{eq} \leqslant 20\delta_o$) for TBLs over rod [24] and cube roughness [21], new fully developed rough wall profiles are formed beyond an initial boundary layer thickness (δ_o) of approximately $23 \sim 30$ in the downstream direction. The slightly longer streamwise distance in the present configuration may be due to relatively smaller initial boundary layer thickness for the longitudinal surface roughness than those for the rod and cube roughness elements, although the roughness height (H/δ) in the present study is larger.

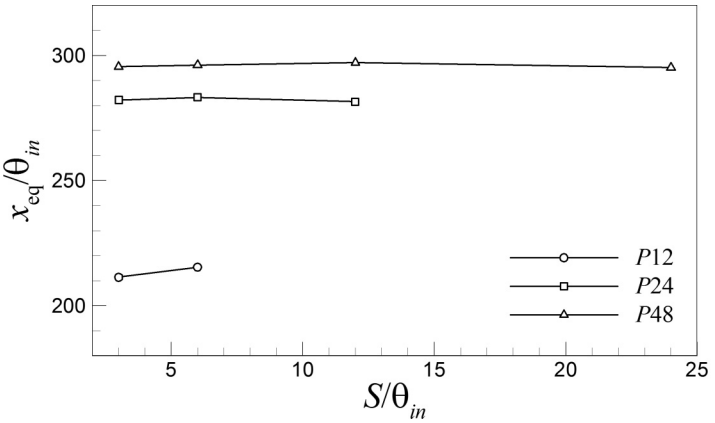

FIG. 6. Streamwise locations required to achieve new equilibrium states after a step change with increases of P and S, normalized by the inlet momentum thickness (θ_{in}).

B. Spatial development of a secondary flow

Before analyzing the characteristics of secondary flows in TBLs over rough walls, the spatial development of a secondary flow in a TBL flow over a longitudinal surface roughness for $P12S3$ is examined in Fig. 7 using isosurfaces of the phase-averaged mean-signed swirling strength

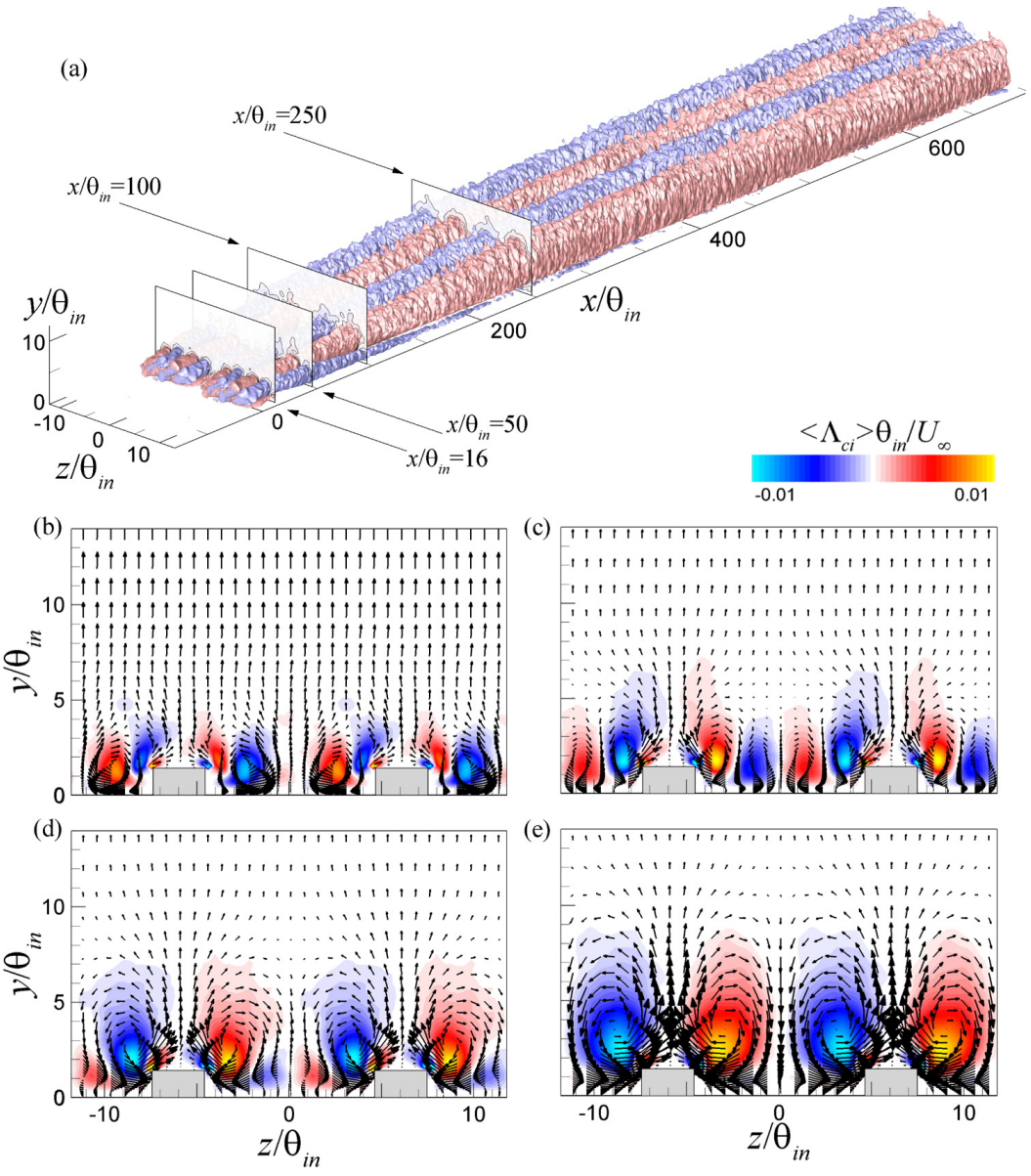

FIG. 7. (a) Isosurfaces of the phase-averaged mean-signed swirling strength ($\langle \Lambda_{ci} \rangle \theta_{in}/U_\infty$) for $P12S3$, showing the formation of a secondary flow throughout the entire turbulent boundary layer with a longitudinal roughness element. Red and blue represent positive and negative values, respectively, and the contour levels are 10% of the maximum and minimum values at $x/\theta_{in} = 250$. The aspect ratio in each direction is (4:1:1). In (b–e), subplots of $\langle \Lambda_{ci} \rangle \delta/U_\infty$ in (a) are drawn on the yz planes with vectors constructed using the phased-averaged mean wall-normal ($\langle v \rangle/U_\infty$) and spanwise velocities ($\langle w \rangle/U_\infty$): (b) $x/\theta_{in} = 16$, (c) 50, (d) 100 and (e) 300.

($\langle \Lambda_{ci} \rangle \theta_{in}/U_\infty$). Here, the signed swirl strength $\Lambda_{ci}(=\lambda_{ci}\omega_x|\omega_x|)$ is computed using the streamwise vorticity ω_x and the swirling strength λ_{ci}, which is defined as the imaginary part of the complex conjugate eigenvalue of the local velocity gradient tensor on the yz plane [25]. The contour levels are 10% of the maximum and minimum values at $x/\theta_{in} = 250$, where the secondary flow reaches an equilibrium state and only one quarter of the computational domain in the spanwise direction is drawn for brevity. In Fig. 7(a), it is clear that the secondary flows spatially develop in the streamwise direction and that two pairs of secondary flow patterns are present in the downstream region of the TBL over the longitudinal surface roughness, occupying the entire boundary layer. In Figs. 7(b)–7(e), subplots of the mean-signed swirling strength with vectors of the phase-averaged mean wall-normal and spanwise velocities on the yz planes provide useful information about how the secondary flows are generated near the step change and developed in the downstream direction. In Fig. 7(b), three types of streamwise vortex pairs are observed near the step change ($x/\theta_{in} = 16$): one vortex pair with the smallest size in the vicinity of the roughness edge, another vortex pair with the largest size in the valley and the third vortex pair, i.e., streamwise vortices of secondary flow, created slightly away from the square edge of the roughness element. The size of the streamwise vortices in the valley is the largest because the main flow, which directly impinges on the roughness element at the location of the step change, creates strong spanwise motions towards the valley. However, as shown in Figs. 7(c) and 7(d), the size and strength of the streamwise vortices in the valley decrease as the flow moves downstream because the spanwise motions originating from the impingement of the flow are gradually reduced in the streamwise direction.

On the other hand, the counter-rotating vortex pair of secondary flows begins to form at either side of the roughness element in Fig. 7(a) and the size of the secondary flow at $x/\theta_{in} = 16$ is smaller than the streamwise vortices in the valley, with weaker strength as well. However, as the flow travels downstream, the volume occupied by the secondary flow increases both in the wall-normal and spanwise directions, indicating that the size of the secondary flow increases in the streamwise direction. Furthermore, the cross-plane view of the secondary flow with an increase of x/θ_{in} in Fig. 7 shows that the strength of the secondary flow also increases in the downstream direction with enhanced spanwise motion toward the roughness in the valley. Note that this spanwise motion associated with the secondary flow is distinct from the spanwise motion observed in the valley due to the impingement of the main flow near the step change [Fig. 7(b)]. The increased spanwise motion for the secondary flow in the valley is deflected by the side wall of the roughness element and creates upwelling motion above the roughness crest. This process of forming the streamwise circulating motion is continuously observed as the secondary flow grows in the streamwise direction. Although the spatial characteristics (i.e., size and strength) of a secondary flow are changed significantly near the step change due to presence of the flow impingement, there is little influence of the step change after about $x/\theta_{in} = 250$, suggesting that the secondary flow is at an equilibrium state, consistent with the observation for the self-preservation of the boundary layer parameters, velocity defect profiles and Reynolds stress profiles in Figs. 4 and 5.

At the equilibrium state [Fig. 7(e)], the counter-rotating streamwise vortices of the secondary flow are predominant in the rough wall TBL. The strong spanwise motions pointing toward each side of the roughness element occupies the entire valley, and the diverging and converging motions observed at elevated and recessed regions, respectively, affect the main flow up to the region for which $y/\delta = 0.65$. The maximum magnitude of the velocities related to the secondary flow on the yz plane is found at the roughness edge irrespective of the streamwise location. The rotational direction of the secondary flow is consistent with previous finding over ridge-type roughness [9,10]. In addition, the presence of small vortices near the roughness edge is consistent with the observation of Vanderwel & Ganapathisubramani [9]. The small vortices in Fig. 7 are continuously observed at the crest edge regardless of the streamwise location, and the strength of the vortices is always greater than that of the secondary flow due to increased velocity gradient at the roughness edge, although the influence of the vortices on the main flow is negligible. Consistent with the findings in the study of Vermaas *et al.* [13], spanwise motions from a high-drag region (a decelerating flow) to a low-drag region (an accelerating flow) are generated near the roughness step change and are reduced as the flow moves downstream. However, these spanwise motions in the present study are diminished along the streamwise direction,

although those motions over strip-type roughness are sustained due to the generation of a secondary flow with a rotational sense, identical to the spanwise motions near the step change.

C. Spatial characteristics of secondary flows

Figures 8 and 9 show the contours of the phase-averaged mean signed swirling strength ($\langle \Lambda_{ci} \rangle \delta / U_\infty$) with vectors constructed using the phased-averaged mean wall-normal ($\langle v \rangle / U_\infty$) and spanwise velocities ($\langle w \rangle / U_\infty$) at regions in equilibrium, $x/\theta_{in} = 512$, as P and S vary in the

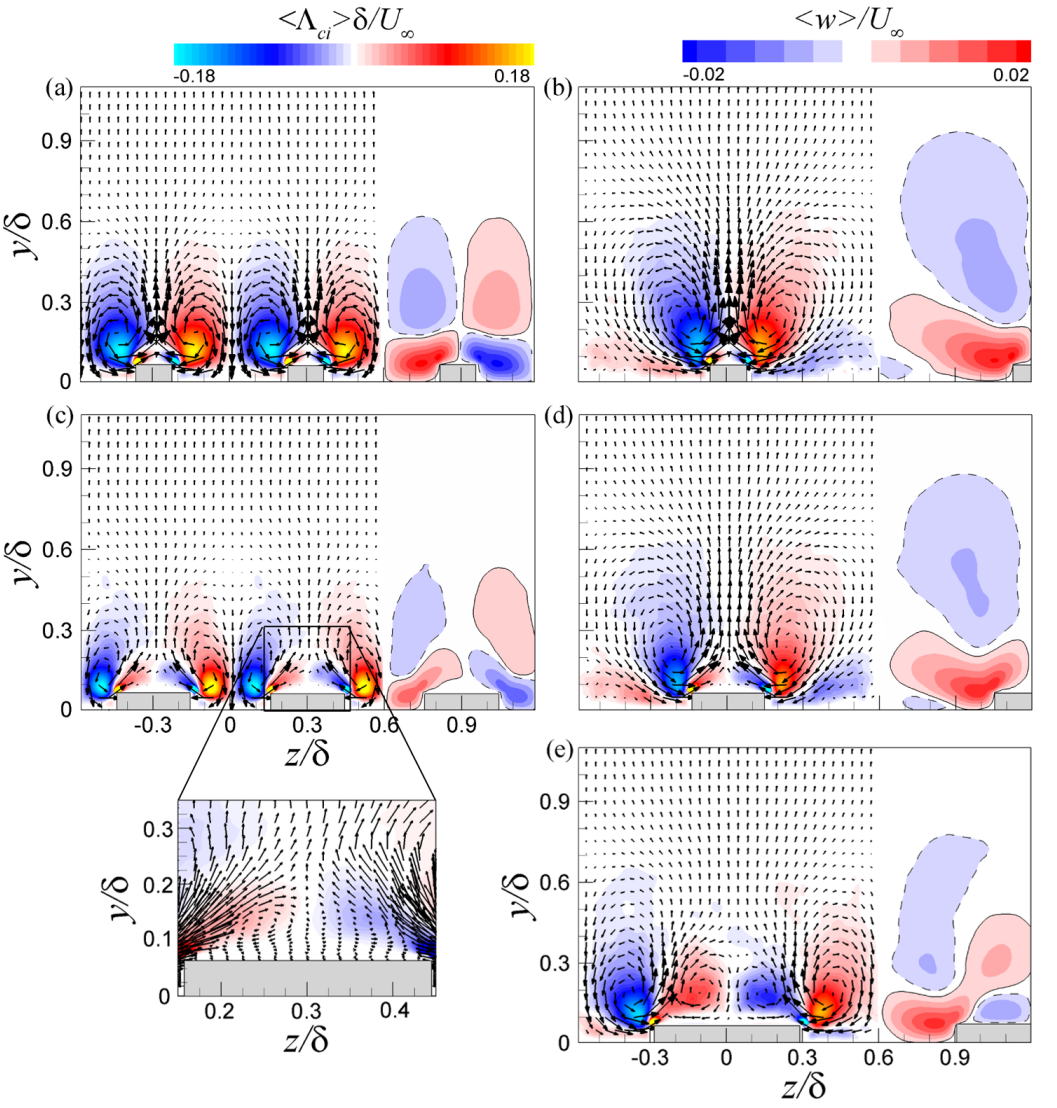

FIG. 8. Contours of the phase-averaged mean-signed swirling strength ($\langle \Lambda_{ci} \rangle \delta / U_\infty$) with vectors constructed using the phased-averaged mean wall-normal ($\langle v \rangle / U_\infty$) and spanwise velocities ($\langle w \rangle / U_\infty$) as P and S vary: (a) $P12S3$ ($P/\delta = 0.58$, $S/\delta = 0.14$), (b) $P24S3$ ($P/\delta = 1.18$, $S/\delta = 0.15$), (c) $P12S6$ ($P/\delta = 0.57$, $S/\delta = 0.27$), (d) $P24S6$ ($P/\delta = 1.18$, $S/\delta = 0.29$) and (e) $P24S12$ ($P/\delta = 1.17$, $S/\delta = 0.59$). On the right in each figure, the phase-averaged mean spanwise velocity ($\langle w \rangle / U_\infty$) is drawn, with line contours of $\langle w \rangle / U_\infty = 0.001$ (solid line) and -0.001 (dashed line) included. The data are extracted in the equilibrium region ($x/\theta_{in} = 512$) for each flow and the vectors are uniformly distributed for clarity.

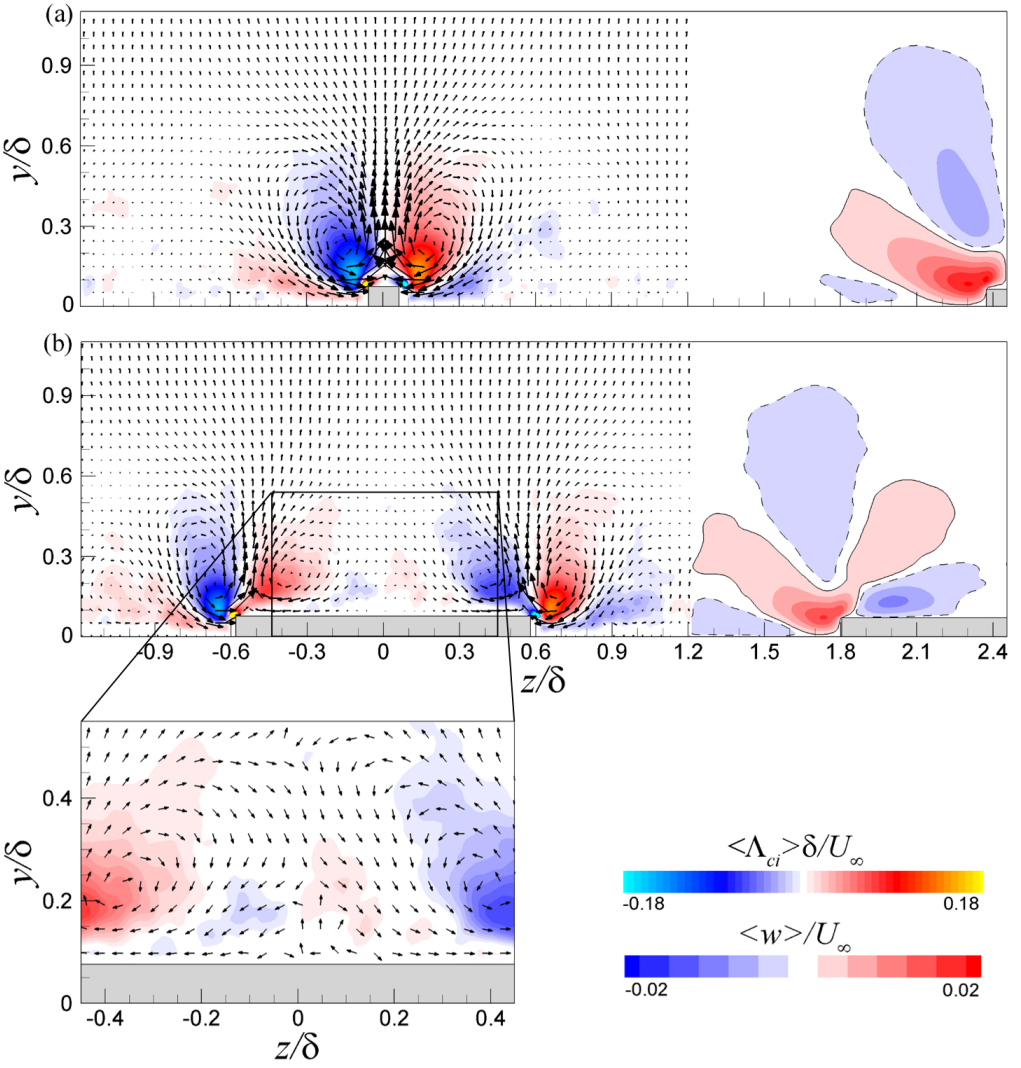

FIG. 9. Identical to those in Fig. 8 but for (a) $P48S3$ ($P/\delta = 2.39$, $S/\delta = 0.15$) and (b) $P48S24$ ($P/\delta = 2.39$, $S/\delta = 1.12$). The data are extracted in the equilibrium region ($x/\theta_{in} = 512$).

corresponding ranges of $12 \leqslant P/\theta_{in} \leqslant 48$ and $3 \leqslant S/\theta_{in} \leqslant 24$. In addition, the contours of the phase-averaged mean spanwise velocity ($\langle w \rangle / U_\infty$) are illustrated on the right in each plot. The boundary layer thickness at the equilibrium location is approximately $\delta/\theta_{in} = 20.5 \pm 0.8$, while P and S vary. In Fig. 8, the presence of secondary flows at the either side of the roughness element is evident for all cases, and the rotational sense of the secondary flows is described as upward motion over the crest and downward motion in the valley, regardless of the values of P and S. Although the Reynolds number is low in the present study, the rotational sense of the secondary flow is consistent with the findings of an experimental study by Vanderwel & Ganapathisubramani [9] at a high Reynolds number. Furthermore, the pitch spacing between the roughness elements ($P/\delta \geqslant 0.5$) is large enough in all cases to induce a large-scale secondary flow over a rough-wall TBL flow [9], and the generated secondary flows affect the mean flow above $y/\delta \geqslant 0.5$.

Although flows with a wide range of P and S values show the generation of the secondary flows over ridge-type roughness, the sizes and strengths of the secondary flows are influenced by the values

of P and S. As the value of S is fixed in Fig. 8, the size of the secondary flows increases with an increase of P, consistent with the observation in Vanderwel & Ganapathisubramani [9]. However, when the value of P is fixed, increasing the value of S leads to a decrease in the size of the secondary flow. Consistent variation of the size of the secondary flow is shown in the velocity contours of $\langle w\rangle/U_\infty$. However, for $P12S3$ shown in Fig. 8(a), a larger secondary flow is formed compared to that of $P12S6$ in Fig. 8(c) despite the fact that the values of P are similar ($P/\delta \approx 0.58$). In addition, although the value of P is sufficiently large for $P24S12$ ($P/\delta = 1.17$, $S/\delta = 0.58$) to create a large-scale secondary flow [9], a relatively small size of the secondary flow for $P24S12$ is observed, as shown in Fig. 8(e). In Fig. 8, because the case for $P12S6$ with the smallest valley width ($P-S$) exhibits the smallest size of the secondary flow with influence up to $y/\delta = 0.5$ [Fig. 8(c)] and the case of $P24S3$ with the largest value of $P-S$ shows the largest secondary flow with influence over $y/\delta > 0.9$ [Fig. 8(b)], it is reasonable to conclude that the valley width ($P-S$) is an important parameter in the determination of the size of the secondary flow over the present ridge-type roughness.

However, the $P48S3$ case in Fig. 9(a) suggests that the size of the secondary flow does not continuously increase as the value of $P-S$ increases, and the size is similar to that for $P24S3$, suggesting that the growth of the secondary flow is limited when the value of $P-S$ exceeds a certain level. The observation that the influence of the secondary flows for $P24S3$ and $P48S3$ exists in the range of $-0.5 \leqslant z/\delta \leqslant 0.5$ indicates that the secondary flow grows in the spanwise direction until its size is comparable to the boundary layer thickness. The importance of the valley width ($P-S$) with regard to the size of the secondary flow is predictable, because the limited valley width restricts the spanwise motions toward the roughness elements to induce the secondary flow. For strip-type roughness, the size of the secondary flow was reported to be proportional to the value of P [6,10]. In addition, for ridge-type roughness with a gradual spanwise change in the bed elevation, the size of the secondary flow is mostly influenced by the value of P [10]. Because strip-type roughness elements do not significantly restrict spanwise motions towards the roughness, contrary to the longitudinal roughness elements, the value of P plays a critical role in determining the sizes of secondary flows.

Willingham *et al.* [6] reported that the strength of the secondary flow is negatively proportional to the width of a high-drag region in TBLs over strip-type roughness based on the maximum magnitude of $\langle \Lambda_{ci}\rangle$. However, as the value of $P/\theta_{in}(=12)$ is fixed, as shown in Fig. 8, the maximum magnitude of $\langle \Lambda_{ci}\rangle\delta/U_\infty$ shows slight increase with an increase in S (as indicated by the color). In addition, the maximum magnitude of $\langle \Lambda_{ci}\rangle\delta/U_\infty$ for $P/\theta_{in} = 24$ is reduced with an increase of S for $S/\theta_{in} < 6$, increasing again for $S/\theta_{in} > 6$. In addition to the inconsistent trend of the strength of the secondary flow noted above, the use of the local magnitude as a means of quantifying the strength of the secondary flow may hinder the broader influence of the secondary flow on the mean flow. Thus, as an alternative approach for assessing the strengths of secondary flows, we consider the mean spanwise velocity field on the cross-plane relative to the flow, similar to an earlier study by Wang & Cheng [10]. As the value of S is fixed in Fig. 8, the strength of $\langle w\rangle/U_\infty$ is intensified with an increase of P, consistent with the findings of Vanderwel & Ganapathisubramani [9] for TBLs with the ridge-type roughness. In addition, when the value of P is fixed, as shown in Fig. 8, the strength of the secondary flow increases with a reduction of S, similar to the observation of Willingham *et al.* [6] in TBLs with strip-type roughness. However, the further increase of P ($P48S3$) in Fig. 9(a) shows that the strength of the secondary flow does not continuously increase with an increase of P, compared to that for $P24S3$ [Fig. 8(b)], although the smaller value of S for $P48S3$ relative to that for $P48S24$ in Fig. 9 exhibits the presence of a stronger secondary flow. The limited increase in the strength of the secondary flow for a sufficiently large P is most likely associated with the variation of the size of the secondary flow. In Fig. 8, the strength of the secondary flow also appears to be related to the valley width ($P-S$) at a fixed value of P; e.g., the strength decreases as the value of $P-S$ decreases, consistent with the variation of the size of the secondary flow. However, a comparison of the secondary flows between $P12S3$ and $P24S12$ [Figs. 8(a) and 8(e)] shows that even when the value of $P-S$ for $P24S12$ is larger, a stronger secondary flow arises for $P12S3$.

In Figs. 8 and 9, it is clear that the spatial characteristics for additional mean streamwise vortices are also affected by the values of P and S. Over the roughness crest, a tertiary flow is shown to be

created as a result of the accumulation of the secondary flow with an increase of S, regardless of the value of P. In addition, the size and strength of the tertiary flow are enhanced with a further increase of S. Wang & Cheng [10] explained that because spanwise motions toward the roughness element in the valley are sharply deflected upward by the side wall, the induced upward motions at either end of the crest lead to the generation of a tertiary flow with a secondary flow over the crest, with the rotational sense of the tertiary flow opposite to the adjacent secondary flow. However, although strong deflections of the spanwise motions are observed for cases with small values of S [Figs. 8(a) and 8(b)], a tertiary flow is not created due to the absence of enough space to make room for the generation of a tertiary flow over the crest. For the cases with $S/\theta_{in} = 6$ [Figs. 8(c) and 8(d)], a tertiary flow based on a vector plot is clearly observed (see the enlarged view in Fig. 8). In addition to the tertiary flow over the roughness crest, an additional tertiary flow is observed in the valley in Figs. 8 and 9. Because the strength of the secondary flow decreases with an increase of S due to the limited spanwise extent for the valley, the tertiary flow in the valley is also weakened. As shown in Fig. 9(b), with a sufficiently large value of S, a quaternary flow created by the induction of the tertiary flow is observed in the middle of the roughness crest based on the $\langle \Lambda_{ci} \rangle$ contours, although the velocity vectors for the quaternary flow are not clear in the enlarged view in Fig. 9. However, because the strength of the tertiary flow in the valley is weaker than that above the roughness crest, clear identification of a quaternary flow in the valley is more difficult [Fig. 9(b)]. For the strip-type roughness, a tertiary flow has not been reported even for large values of P and S due to the relatively weak deflection of the spanwise upward motions [6,10]. In addition, Although Türk *et al.* [15] and Stroh *et al.* [14] reported that the rotational sense of the secondary flow is reversed by the formation of a strong tertiary flow with sufficiently large P and S values over SHSs, the rotational sense over the ridge-type roughness is invariant with respect to the values of P and S due to the emergence of a weak tertiary flow caused by the induction of the secondary flow.

Figure 10 shows the contours of the phase-averaged mean streamwise velocity ($\langle v \rangle / U_\infty$) with vectors constructed using the phased-averaged mean wall-normal ($\langle v \rangle / U_\infty$) and spanwise velocities ($\langle w \rangle / U_\infty$) as P and S vary. The data are extracted in the equilibrium region ($x/\theta_{in} = 512$) for each

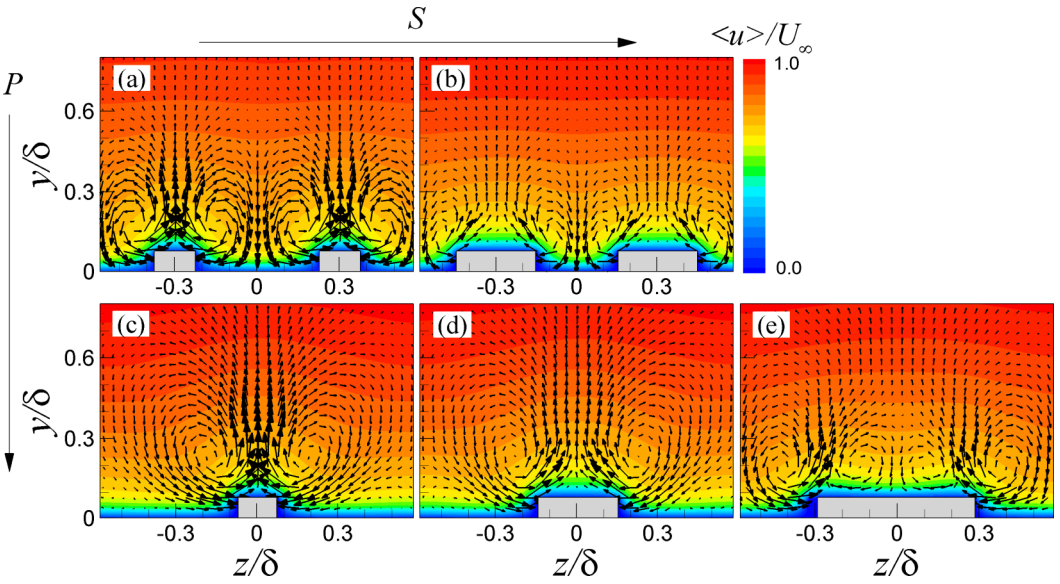

FIG. 10. Contours of the phase-averaged mean streamwise velocity ($\langle u \rangle / U_\infty$) with vectors constructed using the phased-averaged mean wall-normal ($\langle v \rangle / U_\infty$) and spanwise velocities ($\langle w \rangle / U_\infty$) while varying P and S: (a) $P12S3$, (b) $P12S6$, (c) $P24S3$, (d) $P24S6$ and (e) $P24S12$. The data are extracted in the equilibrium region ($x/\theta_{in} = 512$) for each flow and the vectors are uniformly distributed for clarity.

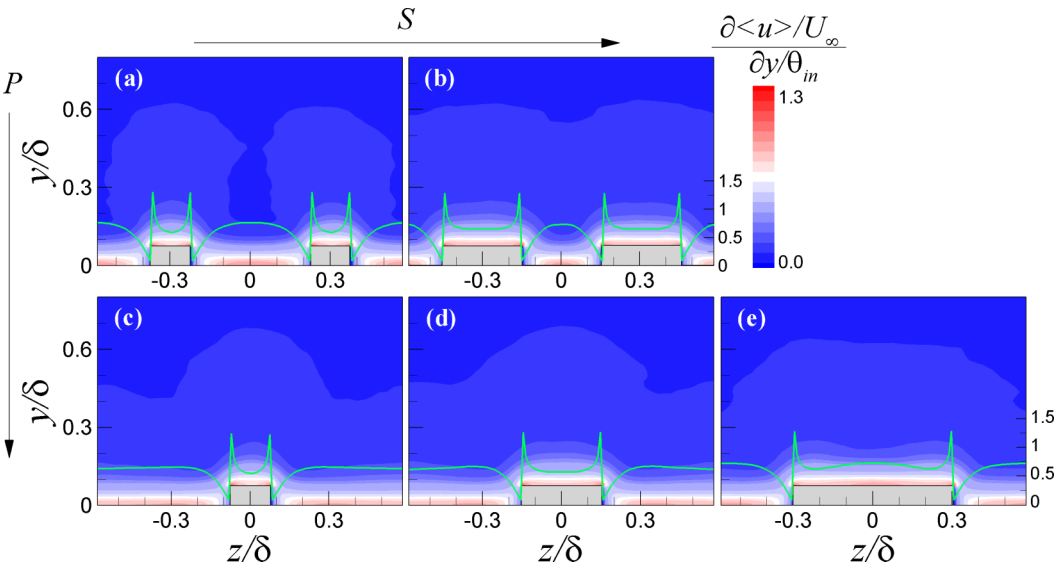

FIG. 11. Contours of the wall-normal gradient of phase-averaged mean streamwise velocity $(\partial\langle u\rangle/\partial y)$ normalized by U_∞/θ_{in} as P and S vary: (a) $P12S3$, (b) $P12S6$, (c) $P24S3$, (d) $P24S6$ and (e) $P24S12$. The data are extracted in the equilibrium region ($x/\theta_{in} = 512$). In each figure, the spanwise variation for the wall-normal gradient of the phase-averaged mean streamwise velocity at the wall $(\partial\langle u\rangle/\partial y)_w$ is included (green line). The label for $(\partial\langle u\rangle/\partial y)_w$ is plotted in the right-hand side of the figures.

flow. In the figures, spanwise heterogeneity of the streamwise velocity is clearly observed, and the spatial pattern is very similar to that in the previous experimental observation of the ridge-type roughness [9,10]. In addition, except for the cases with sufficiently large values of P and S, the occurrence of the upward (downward) motion in the region for the LMP (HMP) is consistent with the previous findings [6,7,9,12] irrespective of the type of roughness. However, the rotational direction of the secondary flows over the ridge-type roughness is opposite to that in earlier observations over strip-type roughness [6,10,11]. In a flow with an isolated riblet, Goldstein and Tuan [16] showed that the secondary flow in the spanwise heterogeneous surface condition determines the distortion of the mean flow heterogeneity of the streamwise velocity, whereas Vanderwel & Ganapathisubramani [9] reported that the retardation of the flow by the surface roughness creates mean flow heterogeneity in the spanwise direction. In contrast to the contours shown in Figs. 10(a)–10(d), the velocity contour in Fig. 10(e) for $P24S12$ indicates that the streamwise velocity pattern above the roughness crest is slightly distorted downward with a downwelling motion, although upward distortion is continuously expected above the roughness crest. Because distortion of the velocity is mainly induced by the presence of the tertiary flow, the secondary flow, which leads to the generation of the tertiary flow over the crest, plays an important role in the generation of the mean flow heterogeneity of the streamwise velocity in the TBLs with the ridge-type roughness. It is noted that although the contour of the streamwise velocity above the crest is distorted downward for $P24S12$, LMPs are still observed over the crest with the downward motion.

To determine the rotational sense of the secondary flow and spanwise locations for LMPs and HMPs, previous studies emphasized the importance of spanwise heterogeneity of the wall shear stress imposed by the roughness [6,9,10,12]. In Fig. 11, contours for the wall-normal gradient of phase-averaged mean streamwise velocity $(\partial\langle u\rangle/\partial y)$ normalized by U_∞/θ_{in} are plotted as P and S vary. In each figure, the spanwise variation for the wall-normal gradient of the phase-averaged mean streamwise velocity at the wall $(\partial\langle u\rangle/\partial y)_w$ is included (green line). Large values of the wall shear stress are observed both over the roughness crest and in the valley, and the maximum values of the wall shear stress always occur at the crest ends, even when the values of P and S are sufficiently

large. On the contrary, small values of the wall shear stress are observed at the bottom wall (near the roughness). The inconsistent behavior of the wall-normal motions at the large drag region with the strip-type roughness (Figs. 7–10), suggests that the generation of the secondary flow over ridge-type roughness is not simply due to the downward motions at this region created by large values of the wall shear stress. The presence of greater wall shear stress on the crest than that in the valley is consistent with earlier results for flows with riblets [16].

D. Formation mechanism of secondary flows over ridge-type roughness

The previous sections show that the rotational sense of a secondary flow for the ridge-type roughness is opposite to the rotational sense for the strip-type roughness [7,10–13]. To examine the physical mechanism driving the secondary flow for the ridge-type roughness, we analyze the Reynolds-averaged tke transport equation, similar to the procedure used by Hinze [3] and Anderson *et al.* [11]. The Reynolds-averaged tke transport equation is as follows:

$$C_{1,k} + C_{2,k} + C_{3,k} = P_k - \varepsilon_k + T_k + D_k + \Pi_k, \tag{3}$$

where $C_{1,k} = \langle u \rangle \frac{\partial k}{\partial x}$, $C_{2,k} = \langle v \rangle \frac{\partial k}{\partial y}$, $C_{3,k} = \langle w \rangle \frac{\partial k}{\partial z}$, $P_k = -\langle u_i' u_j' \rangle \frac{\partial \langle u_i \rangle}{\partial x_j}$, $\varepsilon_k = \nu \langle \frac{\partial u_i'}{\partial x_j} \frac{\partial u_i'}{\partial x_j} \rangle$, $T_k = -\frac{1}{2} \frac{\partial \langle u_i' u_i' u_j' \rangle}{\partial x_j}$, $D_k = \nu \frac{\partial^2 k}{\partial x_j{}^2}$ and $\Pi_k = -\frac{\partial}{\partial x_j} \frac{\langle u_j' p' \rangle}{\rho}$. For a turbulent flow over spanwise heterogeneous surface roughness, local imbalance of the terms on the right-hand side (RHS) of Eq. (3) is expected on the cross-stream plane; thus, the advection of tke is naturally derived to achieve a local balance between the left- and right-hand sides of Eq. (3) such that the turbulence-poor fluid is transported to a region with high production, whereas the turbulence-rich fluid is transported outward the region. The derived advective velocity is presented as the mean streamwise circulation of a secondary flow in a turbulent flow [3].

Before continuing, the spatial distributions of the Reynolds stresses for the ridge-type roughness (for $P12S3$) are investigated, as shown in Fig. 12. In Fig. 12(a), the contour of the streamwise Reynolds normal stress, $\langle u'u' \rangle$, which contributes to the spatial distribution of tke with a large magnitude, shows that $\langle u'u' \rangle$ has large positive values over the roughness crest due to the high drag of the elevated surface (Fig. 11), with two maximum peaks of $\langle u'u' \rangle$ observed at the either edge of the roughness. The spanwise gradient of $\langle u'u' \rangle$ in the direction from the valley to the roughness element near the spanwise step change is positive. However, because slightly large values of $\langle u'u' \rangle$ (white color) are also found in the valley due to the no-slip surface on the bottom wall, the spanwise gradient of $\langle u'u' \rangle$ in the direction from the valley to the roughness element is negative in this region. The spatial distributions for the wall-normal, $\langle v'v' \rangle$, and spanwise Reynolds stresses, $\langle w'w' \rangle$, in Figs. 12(b) and 12(c) indicate that large values of $\langle v'v' \rangle$ and $\langle w'w' \rangle$ occur above the roughness crest and that the magnitude of $\langle w'w' \rangle$ is greater than that of $\langle v'v' \rangle$. The occurrence of the maximum $\langle w'w' \rangle$ over the crest, where the mean spanwise velocity is zero [Fig. 8(a)], indicates that the instantaneous spanwise velocity from the valley is vigorously deflected across the crest, leading to enhanced spanwise fluctuations above the crest. In Figs. 12(d) and 12(e), the contour of $\langle u'v' \rangle$ reaches its maximum value over the crest, although $\langle u'w' \rangle$ with an opposite sign is enhanced at either side of the roughness elements with a symmetric pattern with respect to the center of the roughness element. Contrary to $\langle u'v' \rangle$ and $\langle u'w' \rangle$, which are intensified by the large value of u', $\langle v'w' \rangle$ in Fig. 12(f) is less organized in space with a low strength, suggesting less impact on the anisotropy of the Reynolds stresses. The distributions of the Reynolds stresses over the ridge-type roughness are in good agreement with previous experimental results by Vanderwel & Ganapathisubramani [9].

To investigate the local imbalance of the RHS in the Reynolds-averaged tke transport equation, all budget terms in the RHS of Eq. (3) and sums of the budget terms are analyzed for $P12S3$ (left) and $P24S12$ (right) in Figs. 13 and 14. For $P12S3$, a high rate of production for tke is observed over the roughness crest and in the valley, and the maximum value of P_k is located slightly away from the either edge of the roughness element [Fig. 13(a)]. The distribution of P_k similar to the contours of $\partial \langle u \rangle / \partial y$ and $\langle u'u' \rangle$ in Fig. 11(a) and Fig. 12(a) indicates that significant contribution of P_k comes from both

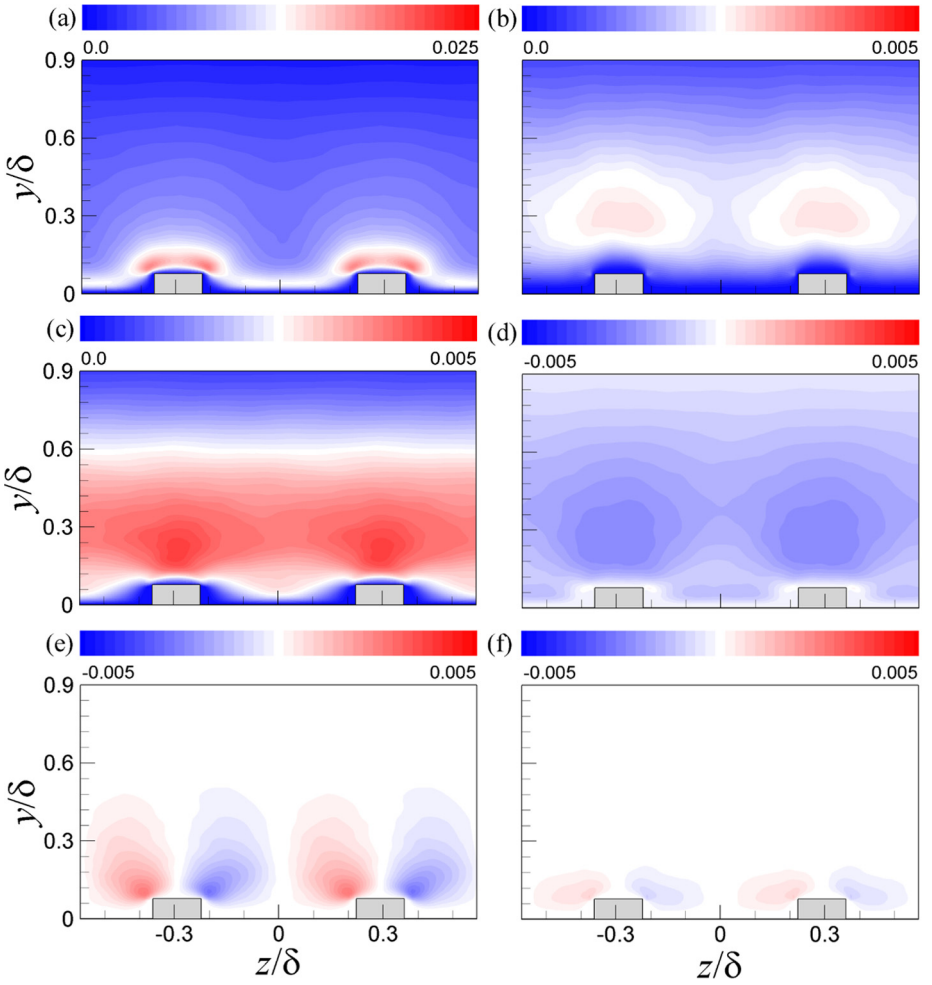

FIG. 12. Contours of the Reynolds stresses for $P12S3$ normalized by U_∞^2: (a) $\langle u'u' \rangle$, (b) $\langle v'v' \rangle$, (c) $\langle w'w' \rangle$, (d) $\langle u'v' \rangle$, (e) $\langle u'w' \rangle$ and (f) $\langle v'w' \rangle$. The data are extracted in the equilibrium region ($x/\theta_{in} = 512$).

terms. Although the distribution of $-\varepsilon_k$ is similar to that of P_k, the magnitude of P_k is stronger slightly above the wall, resulting in a local imbalance between production and dissipation [Fig. 14(a)], similar to the previous observation over strip-type roughness [11]. However, contrary to the previous finding of Anderson *et al.* [11], it is obvious that the turbulent transport term, T_k, and the viscous diffusion term, D_k, significantly contribute to the local imbalance of the RHS in Eq. (3) over ridge-type roughness. In Figs. 13(e) and 13(g), the values of T_k and D_k are positive on the bottom of the no-slip surface and negative slightly away the wall. Compared to D_k, confined close to the wall, a relatively large value of T_k is observed up to $y/\delta < 0.6$ for all spanwise locations. In Fig. 13(i), the strength of the velocity pressure-gradient term Π_k is relatively small, showing little influence on the energy budget tke over the ridge-type roughness, similar to that over strip-type roughness. Compared to the contour of $P_k - \varepsilon_k$ [Fig. 14(a)], the distinctive contour pattern of $P_k - \varepsilon_k + T_k + D_k + \Pi_k$ in Fig. 14(c) supports the contention that the sum of $T_k + D_k + \Pi_k$ in Fig. 14(e) is important in the determination of the advection of tke on the yz plane. In Figs. 14(c) and 14(e), the negative transport rates of $T_k + D_k + \Pi_k$ exceed the positive values of $P_k - \varepsilon_k$ over the crest and the positive transport rates in the valley exceed the negative values of $P_k - \varepsilon_k$. In Figs. 13 and 14, the overall spatial distributions of the tke budget terms and sums of the budget terms for $P24S12$ are similar to those for $P12S3$,

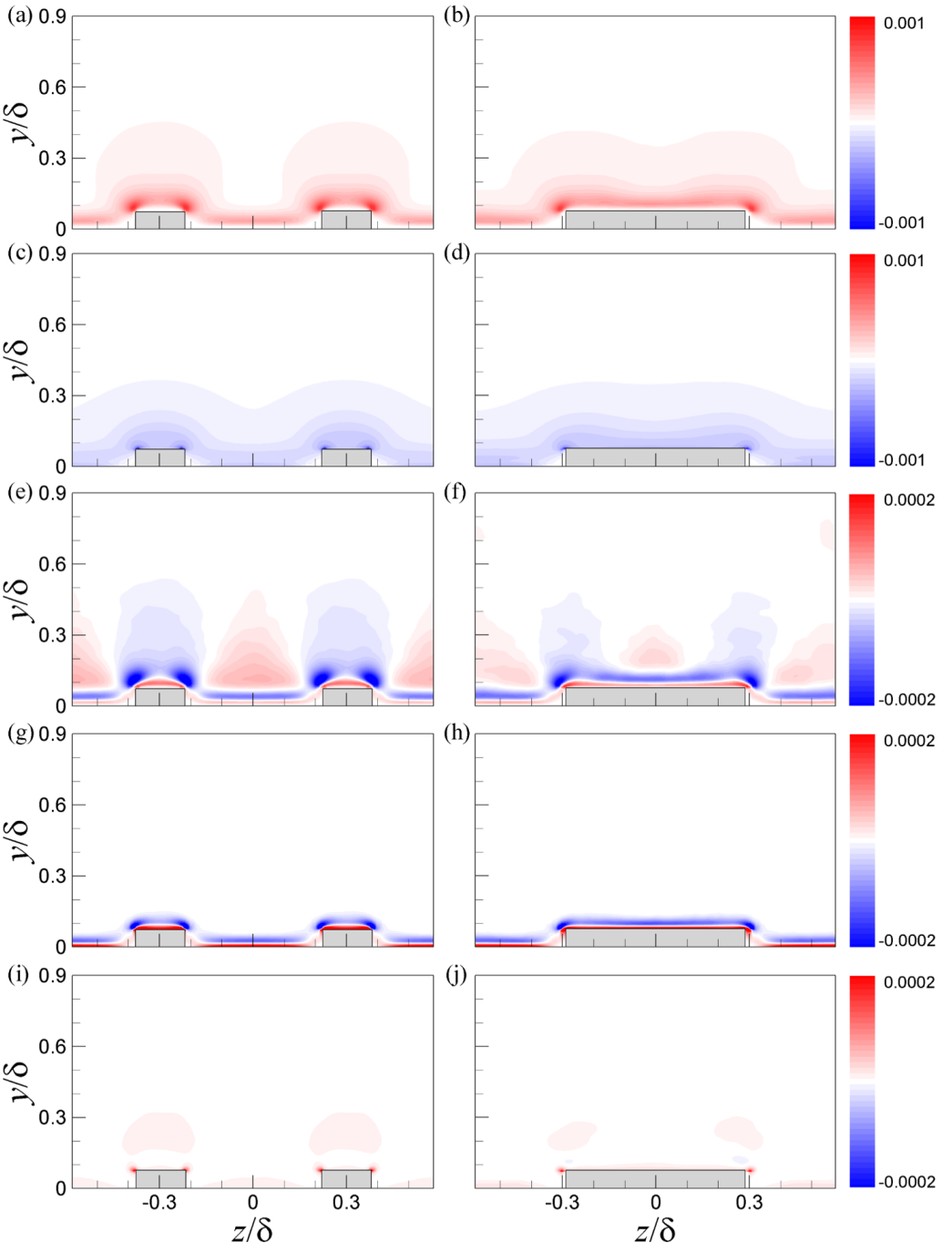

FIG. 13. Contours of budget terms for the turbulent kinetic energy: (a, b) production term, P_k, (c, d) dissipation term, $-\varepsilon_k$, (e, f) turbulent transport term, T_k, (g, h) viscous diffusion term, D_k, and (i, j) velocity pressure-gradient term, Π_k. (a, c, e, g, i) $P12S3$ and (b, d, f, g, h) $P24S12$. The data are extracted in the equilibrium region ($x/\theta_{in} = 512$) for each flow.

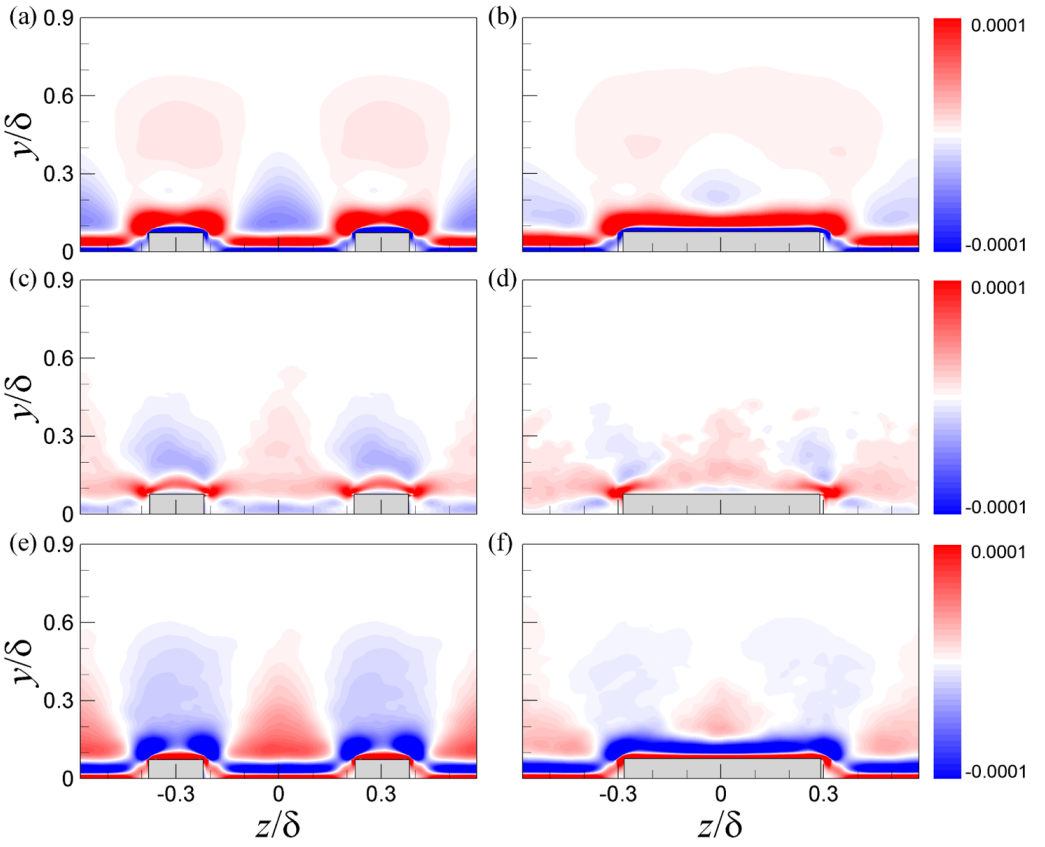

FIG. 14. Contours of (a, b) the sum of the turbulent kinetic energy production and dissipation terms, $P_k - \varepsilon_k$, (c, d) the sum of all turbulent kinetic energy budget terms, $P_k - \varepsilon_k + T_k + D_k + \Pi_k$ and (e, f) the sum of the turbulent transport, viscous diffusion and velocity pressure-gradient terms, $T_k + D_k + \Pi_k$. (a, c, e) $P12S3$ and (b, d, f) $P24S12$. The data are extracted in the equilibrium region ($x/\theta_{in} = 512$).

except that a positive $T_k + D_k + \Pi_k$ is observed above the roughness crest for $P24S12$ due to the positive T_k.

The comparison of the contours of T_k, D_k and Π_k in Figs. 13 and 14 indicates that the dominant contribution to the sum of $T_k + D_k + \Pi_k$ comes from large value of T_k throughout the region near the roughness. To examine how the term of T_k is created over the ridge-type roughness in detail, contours of the turbulent transport terms in the wall-normal and spanwise directions for $P12S3$ are plotted in Fig. 15 with the contours of the dominant triple-product terms of the velocity fluctuations. Here, we assume that the streamwise gradient of the averaged quantities is relatively small; thus, the turbulent transport term stemming from the streamwise velocity fluctuation u' (i.e., $-1/2\partial\langle u_i' u_i' u'\rangle/\partial x$) is neglected in the analysis. In Figs. 15(a) and 15(c), it is clear that the wall-normal transport rate of the streamwise turbulent kinetic energy plays a dominant role in the creation of the wall-normal transport of tke within the entire boundary layer due to the large magnitude of u'. Similarly, the spanwise transport of tke in Fig. 15(b) is mostly induced by the spanwise transport of the streamwise kinetic energy in Fig. 15(d). In Fig. 15(e), transport of the streamwise turbulent kinetic energy [Fig. 12(a)] in the upward direction caused by the positive v' (red) is observed both over the roughness crest and in the valley, and only small portion of the negative $\langle u'u'v'\rangle$ is found near the no-slip surface (blue).

The positive and negative transports of the streamwise turbulent kinetic energy are closely associated with the generation of the large energy production P_k at the boundary between the positive

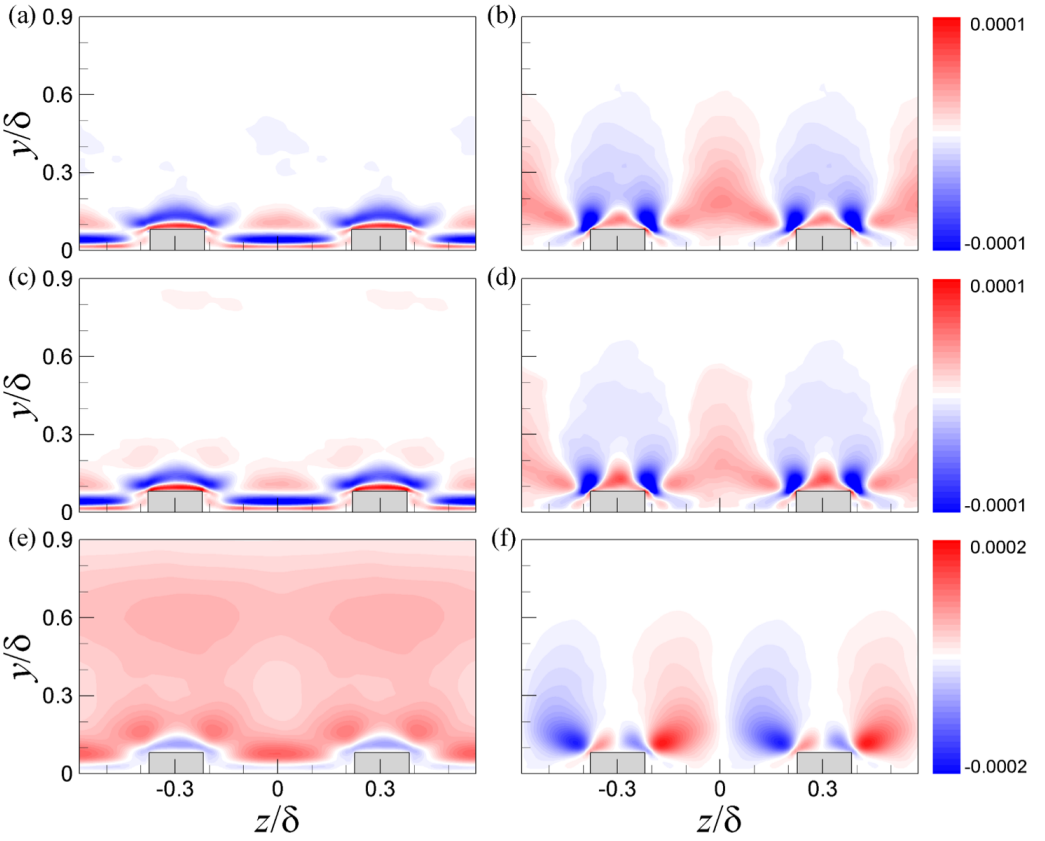

FIG. 15. Contours of the turbulent transport term: (a) $-1/2(\partial\langle u'u'v'\rangle/\partial y + \partial\langle v'v'v'\rangle/\partial y + \partial\langle w'w'v'\rangle/\partial y)$, (b) $-1/2(\partial\langle u'u'w'\rangle/\partial z + \partial\langle v'v'w'\rangle/\partial z + \partial\langle w'w'w'\rangle/\partial z)$, (c) $-1/2\partial\langle u'u'v'\rangle/\partial y$, (d) $-1/2\partial\langle u'u'w'\rangle/\partial z$, (e) $\langle u'u'v'\rangle$ and (f) $\langle u'u'w'\rangle$, normalized by U_∞^3/θ_{in} for $P12S3$. The data are extracted in the equilibrium region ($x/\theta_{in} = 512$).

and negative contours of $\langle u'u'v'\rangle$ [see Fig. 13(a)]. When the values of $\langle u'u'v'\rangle$ change from negative to positive above the wall, the term of $-1/2\partial\langle u'u'v'\rangle/\partial y$ is strongly negative, whereas the term of $-1/2\partial\langle u'u'v'\rangle/\partial y$ is positive near the roughness crest. In Fig. 15(f), considerable transport of the turbulent streamwise kinetic energy by w' in the direction from the crest to the valley is observed on the transverse plane while relatively minor transport of the streamwise kinetic energy pointing to the roughness center is found right above the crest. Similar to the observation for $\langle u'u'v'\rangle$, the spatial distribution of $\langle u'u'w'\rangle$ is linked to P_k [Fig. 13(a)], because the large production rate P_k above the crest leads to positive and negative energy transport in the spanwise direction. In Fig. 15(d), a large portion of negative $-1/2\partial\langle u'u'w'\rangle/\partial z$ above the crest is observed when the values of $\langle u'u'w'\rangle$ change from negative to positive across the region above the crest, whereas a positive $-1/2\partial\langle u'u'w'\rangle/\partial z$ is found in the valley and above the crest when the values of $\langle u'u'w'\rangle$ change from positive to negative. Considering the contribution of T_k to the RHS, which is important to derive the advection of tke, the negative value of the RHS over the crest and on the bottom of the valley results from $-1/2\partial\langle u'u'v'\rangle/\partial y$ and $-\varepsilon_k$ while the positive value of the RHS in the valley comes from $-1/2\partial\langle u'u'w'\rangle/\partial z$, $-1/2\partial\langle u'u'v'\rangle/\partial y$ and P_k.

Based on the observation of the terms $\langle u'v'\rangle$ and $\langle u'w'\rangle$ in Figs. 12(d) and 12(e), the positive value of $\langle u'u'v'\rangle$ over the crest in Fig. 15 indicates that u' is correlated with a positive v'. The presence of the negative value of $\langle u'v'\rangle$ over the crest in Fig. 12 suggests that the combination of the negative u'

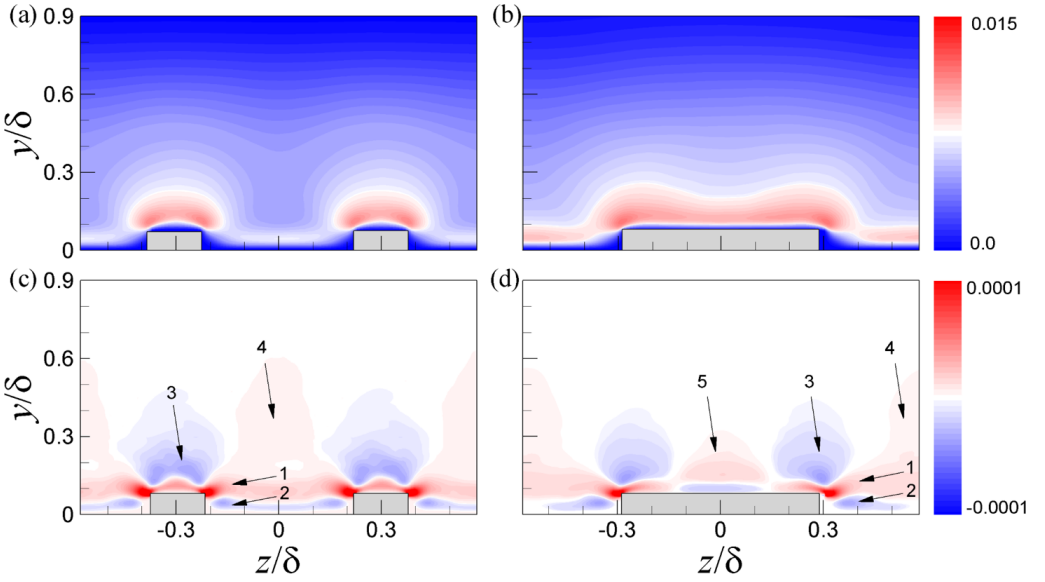

FIG. 16. Contours of (a, b) the turbulent kinetic energy and (c, d) the sum of the convective terms ($C_{2,k} + C_{3,k}$). (a, c) $P12S3$ and (b, d) $P24S12$. The data are extracted in the equilibrium region ($x/\theta_{in} = 512$).

and the positive v' are dominant in this region. Likewise, the opposite signs of $\langle u'u'w' \rangle$ at the either side of the roughness element in Fig. 15 show that u' is temporally correlated with w', pointing to the valley from the crest. The opposite sign of $\langle u'w' \rangle$ relative to that of $\langle u'u'w' \rangle$ near the edge of the roughness in Fig. 12 suggests that the combination of the negative u' and w' pointing towards the valley is dominant. Thus, when the large streamwise turbulent kinetic energy strongly related to the negative u' is transported near roughness, the upward v' contributes to the generation of the active transport of tke around the roughness element with w' toward the valley. On the other hand, the secondary flow convects the negative u'structure (low-speed fluid) along the roughness up over the crest and brings the positive u'structure (high-speed fluid) down toward the wall on either side of the roughness. The region of upflow is clearly associated with increased levels of $\langle u'u' \rangle$ and $\langle -u'v' \rangle$.

Figure 16 shows the contours of tke and the sum of the convective terms in Eq. (3) for $P12S3$ and $P24S12$, respectively. Here, the streamwise gradient of tke is neglected at a local streamwise position (i.e., $C_{1,k} \approx 0$) due to the small contribution. The contour of tke in Fig. 16(a) is half of the sum of the Reynolds normal stresses in Fig. 12 (i.e., $1/2\langle u_i' u_i' \rangle$), and the dominant tke is observed above the roughness crest. In Figs. 16(c) and 16(d), the sum of the convective terms, $C_{2,k} + C_{3,k}$ for $P12S3$ and $P24S12$ is balanced with the RHS in Figs. 14(c) and 14(d). Because the spanwise gradient of tke is negative in region "1" in Fig. 16(a) mostly due to the spanwise variation of $\langle u'u' \rangle$ in Fig. 12(a), the presence of the positive RHS in region "1" in Fig. 16(c) indicates that the spanwise advective velocity should be negative in this region; that is, the flow should point to the roughness element from the valley. It should also be noted that although the term of $C_{2,k}$ may contribute to the positive value in region "1," the dominant contribution comes from the term $C_{3,k}$, as shown in Fig. 8(a). Similarly, the spanwise gradient of tke in region "2" is positive; thus, the spanwise advective velocity should be negative to satisfy the requirements for the convective term to be negative in this region. For the wall-normal advective velocity, a negative RHS and a positive RHS exist at regions "3" and "4," respectively, with a negative wall-normal gradient of tke in both regions. Thus, the positive wall-normal advective velocity is derived at region "3," while the negative wall-normal advective velocity is induced at region "4." In Fig. 16(d), a similar driving mechanism for the wall-normal and spanwise velocities is observed at the equivalent regions of "1–4" for $P24S12$. However, the positive convective term is induced with an increase of S at region "5" and the negative wall-normal

advective velocity is derived with the negative wall-normal gradient of tke in this region. With the previous observation in Figs. 8(a) and 8(e), the present results demonstrate that the generation of a secondary flow and a tertiary flow over the ridge-type roughness can be explained as the realization of the wall-normal and spanwise advective velocities derived by the local imbalance of the RHS in Eq. (3); thus, the generated secondary and tertiary flows over the ridge-type roughness belongs to Prandtl's secondary flow of the second kind.

Finally, it is worth further discussing the origin of the opposite sense of rotation for the secondary flows between the ridge- and strip-type roughness elements. Although the contours of $P_k - \varepsilon_k$ for the ridge- and strip-type roughness show distinctive patterns near the bottom wall (see Fig. 7 in Ref. [11]), similar spatial patterns for $P_k - \varepsilon_k$ are observed for the both types far from the wall, i.e., a positive value of $P_k - \varepsilon_k$ above the high-drag region and a negative value of $P_k - \varepsilon_k$ above the low-drag region. However, because the positive value of $P_k - \varepsilon_k$ with the negative wall-normal gradient of tke induces a downward advective velocity above the high-drag region, the wall-normal advective velocity resulting from $P_k - \varepsilon_k$ in the present study does not correspond to that of the generated secondary flow over the ridge-type roughness. Thus, in addition to the local imbalance of $P_k - \varepsilon_k$, the contribution of the turbulent transport term, T_k, to the induction of the secondary flow is required to explain the rotational sense of the secondary flow for the ridge-type roughness, contrary to the turbulent transport term being less important for the strip-type roughness [11]. Because the presence of the ridge-type roughness leads to considerable energy production above the roughness crest, in particular near the roughness edge [Fig. 13(a)] due to the large velocity gradient (Fig. 7), the active transport of the streamwise turbulent energy in the wall-normal and spanwise directions results in a large transport term (Fig. 15). Although a large amount of energy production of tke is also found in TBLs in a high-drag region over the strip-type roughness [11], the energy production is less intense over the strip-type roughness and the energy transport over the strip-type roughness by T_k is highly limited in the near-wall region due to the small elevation for a high-drag region, similar to that in a smooth wall turbulent flow [26].

Although the generation of the active turbulent transport in TBLs over ridge-type roughness is explained using the energy imbalance near the roughness, an additional physical mechanism that causes the secondary flow with the corresponding rotational sense can come into play. In a turbulent flow with an isolated riblet, Goldstein & Tuan [16] showed that secondary flows arise due to the upward deflection of spanwise fluctuations, as numerical simulations of turbulent flows over wires and with only a w-damping fin produced strong secondary flows. The presence of the wires to impose the effects of the triangular riblet crest (or edge) and the w-damping fin to prevent the flow through the fin significantly damped the spanwise flows and deflected them vertically. In Figs. 8 and 9, although the upward motions over the roughness crest and downward motions in the valley are affected by the values of P and S due to the existence of the tertiary and quaternary flows for the ridge-type roughness, dominant spanwise motions toward the roughness element in all cases are observed in the valley, with cores of secondary flows near abrupt spanwise step changes. These results suggest that the deflection of the spanwise motions due to damping by the spanwise step change is crucial to generate the active turbulent transport with the corresponding secondary flows over the ridge-type roughness. However, for strip-type roughness, the damping of the cross-flow fluctuations is not significant near the boundary between high- and low-drag regions due to the relatively small difference in elevation between the elevated and recessed topographies. The strong deflection of the spanwise motions by the spanwise step change is consistent with the observation of the small vortices at the crest edge (Fig. 8).

In an experimental study of a TBL with a three-dimensional multiscale roughness topology, Barros and Christensen [7] also showed that the spanwise gradient of the roughness height excites a secondary flow in the form of streamwise-elongated roll cells, which then induce spanwise-alternating LMP and HMP patterns. However, the mean roughness height in their study was $H/\delta = 0.045$, and this value is similar to the value ($H/h_m = 0.034$) of sediment particles (strip-type roughness) in an experiment with an open channel flow, where h_m is the mean flow depth [10]. These smaller roughness heights for the strip-type roughness than that ($H/\delta \approx 0.08$) of the present longitudinal

surface roughness in the equilibrium state for $P12S3$ weaken the effects of the large spanwise step change between the high- and low-drag regions observed in the present study and the roughness topology for the strip-type roughness does not play a role in generating the effects of the roughness edge (e.g., the square edge or triangular edge) for the induction of the upwash flow over the crest due to the less intense turbulent transport near the roughness. It should be noted that although the strip-type roughness employed by Wang & Cheng [10] and Anderson *et al.* [11] was characterized by periodic spanwise patterns of high and low roughness, that in Barros & Christensen [7] was replicated from a damaged turbine blade containing a broad range of topographical scales in a highly irregular manner on the entire wall.

IV. SUMMARY AND CONCLUSION

In the present study, we conducted DNSs of TBL flows over longitudinal roughness elements to examine the spatial characteristics of secondary flows and the associated mean flow heterogeneity as P and S vary. Based on the streamwise variation of the TBL parameters and the profiles of the velocity defect forms and Reynolds stresses, the establishment of self-preservation for rough-wall TBLs is observed at approximately $x/\theta_{in} > 220$ for all cases. As rough-wall TBLs spatially develop along the streamwise direction, a secondary flow is generated as a pair of counter-rotating vortices at either side of the roughness from the step change near the inlet, and the size and strength of the secondary flow grow with increased spanwise motions toward the roughness element along the downstream direction, although the secondary flow reaches the equilibrium state at the streamwise location similar to the observation of self-preservation of rough-wall TBLs.

As the values of P and S vary in the TBLs over ridge-type roughness, the spatial characteristics of the secondary flows are compared in states of equilibrium. The sizes of the secondary flows are mostly determined by the value of $P-S$ (i.e., valley width), because the amount of spanwise motion for secondary flows is less restricted with an increase of the valley width. On the other hand, the strength of the secondary flows is enhanced when the value of P increases and the value of S decreases, indicating that the strengths of the secondary flows are not proportional to the sizes of these flows. As the value of S increases, a tertiary flow emerges over the roughness crest as a result of the accumulation of the secondary flow, and the size and strength of the tertiary flow is enhanced with an increase of S. Because the tertiary flow arising over the crest is stronger than that in the valley due to the presence of strong upward motions at the ends of the crest, a quaternary flow is also induced over the crest for a sufficiently large value of S. Although the sizes and strengths of the secondary flows and the additional tertiary and quaternary flows are affected by the roughness configuration, the rotational direction of the secondary flows and the spanwise locations for the LMPs and HMPs are consistent regardless of the values of P and S; the LMP occurs over the crest and the HMP arises in the valley. The distributions of the mean streamwise velocity and wall shear stress show that the secondary flow plays an important role in the generation of the mean flow heterogeneity of the streamwise velocity in TBLs over the ridge-type roughness and that the generation of the secondary flow over the ridge-type roughness is not simply due to the downward motions created by the large wall shear stress.

To examine the origin of the opposite rotational sense of secondary flows between the ridge- and strip-type roughness elements, we analyze the Reynolds-averaged tke transport equation. It was shown that the local imbalance of the RHS in the equation resulting from the spanwise heterogeneity of the surface condition determines the advective velocities of tke on the cross-stream plane. When the wall-normal gradient of tke is negative, the negative RHS in the region with a large amount of drag should determine the upward advective velocity and the positive RHS in the low-drag region should derive the downward advective velocity. Similarly, when the spanwise gradient of tke is positive and negative, the spanwise advective velocity should be negative to be balanced with the negative and positive RHS terms. Therefore, the secondary flow generated over ridge-type roughness is due to Prandtl's secondary flow of the second kind, which is initiated and sustained by the anisotropy of turbulence. The distinctive rotational sense of secondary flows with respect to the roughness type

is primarily attributed to the significant contribution of the turbulent transport term in the energy budget for the ridge-type roughness, whereas this is not the case for the strip-type roughness. The large contribution of the turbulent transport for the ridge-type roughness is closely associated with the active energy production of tke near the roughness edge. The active transport of tke for the ridge-type roughness is a direct consequence of the upward deflection of the spanwise motions in the valley mostly caused by the roughness edge, creating strong positive v' motions above the crest and w' motions toward the valley.

ACKNOWLEDGMENTS

This research was supported by the National Research Foundation of Korea (NRF) funded by the Ministry of Education (Grant No. NRF-2017R1D1A1A09000537) and the Ministry of Science, ICT & Future Planning (Grant No. NRF-2017R1A5A1015311).

[1] J. Nikuradase, Turbulente Strömung in nicht kreisförmigen Rohren, Ing.-Arch. **1**, 306 (1930).
[2] L. Prandtl, *Essentials of Fluid Dynamics* (Blackie, London, 1952).
[3] J. Hinze, Secondary currents in wall turbulence, Phys. Fluids (Suppl.) **10**, S122 (1967).
[4] J. Hinze, Experimental investigation on secondary currents in the turbulent flow through a straight conduit, Appl. Sci. Res. **28**, 453 (1973).
[5] H. Perkins, The formation of streamwise vorticity in turbulent flow, J. Fluid Mech. **44**, 721 (1970).
[6] D. Willingham, W. Anderson, K. T. Christensen, and J. Barros, Turbulent boundary layer flow over transverse aerodynamic roughness transitions: Induced mixing and flow characterization, Phys. Fluids **26**, 025111 (2013).
[7] J. M. Barros and K. T. Christensen, Observations of turbulent secondary flows in a rough-wall boundary layer, J. Fluid Mech. **748**, R1 (2014).
[8] R. Mejia-Alvarez and K. Christensen, Wall-parallel stereo PIV measurements in the roughness sublayer of turbulent flow overlying highly-irregular roughness, Phys. Fluids **25**, 115109 (2013).
[9] C. Vanderwel and B. Ganapathisubramani, Effects of spanwise spacing on large-scale secondary flows in rough-wall turbulent boundary layers, J. Fluid Mech. **774**, R2 (2015).
[10] Z.-Q. Wang and N.-S. Cheng, Time-mean structure of secondary flows in open channel with longitudinal bedforms, Adv. Water Resour. **29**, 1634 (2006).
[11] W. Anderson, J. M. Barros, K. T. Christensen, and A. Awashi, Numerical and experimental study of mechanisms responsible for turbulent secondary flows in boundary layer flows over spanwise heterogeneous roughness, J. Fluid Mech. **768**, 316 (2015).
[12] T. Stoesser, R. McSherry, and B. Fraga, Secondary currents and turbulence over a non-uniformly roughened open channel bed, Water **7**, 4896 (2015).
[13] D. Vermaas, W. Uijttewall, and A. Hoitink, Lateral transfer of streamwise momentum caused by a roughness transition across a shallow channel, Water Resour. Res. **47**, W02530 (2011).
[14] A. Stroh, Y. Hasegawa, J. Kriegseis, and B. Frohnapfel, Secondary vortices over surfaces with spanwise varying drag, J. Fluid Mech. **17**, 1142 (2016).
[15] S. Türk, G. Daschiel, A. Stroh, Y. Hasegawa, and B. Frohnapfel, Turbulent flow over superhydrophobic surfaces with streamwise grooves, J. Fluid Mech. **747**, 186 (2014).
[16] D. B. Goldstein and T.-C. Tuan, Secondary flow induced by riblets, J. Fluid Mech. **363**, 115 (1998).
[17] K. Kim, S.-J. Baek, and H. J. Sung, An implicit velocity decoupling procedure for the incompressible Navier–Stokes equations, Intl J. Numer. Methods Fluids **38**, 125 (2002).
[18] J. Kim, D. Kim, and H. Choi, An immersed boundary finite-volume method for simulations of flow in complex geometries, J. Comput. Phys. **171**, 132 (2001).
[19] T. S. Lund, X. Wu, and K. D. Squires, Generation of turbulent inflow data for spatially developing boundary layer simulation, J. Comput. Phys. **140**, 233 (1998).

[20] P. R. Spalart, Direct simulation of a turbulent boundary layer up to Reθ = 1410, J. Fluid Mech. **187**, 61 (1988).
[21] J. H. Lee, H. J. Sung, and P.-Å. Krogstad, Direct numerical simulation of the turbulent boundary layer over a cube-roughened wall, J. Fluid Mech. **669**, 397 (2011).
[22] A. E. Perry, W. H. Schofield, and P. N. Joubert, Rough wall turbulent boundary layers, J. Fluid Mech. **37**, 383 (1969).
[23] R. J. Smalley, R. A. Antonia, and L. Djenidi, Self-preservation of rough-wall turbulent boundary layers, Eur. J. Mech. B – Fluids **20**, 591 (2001).
[24] S. H. Lee and H. J. Sung, Direct numerical simulation of the turbulent boundary layer over a rod-roughened wall, J. Fluid Mech. **584**, 125 (2007).
[25] J. Zhou, R. J. Adrian, S. Balachandar, and T. M. Kendall, Mechanisms for generating coherent packets of hairpin vortices, J. Fluid Mech. **387**, 353 (1999).
[26] N. N. Mansour, J. Kim, and P. Moin, Reynolds-stress and dissipation rate budgets in a turbulent channel flow, J. Fluid Mech. **194**, 15 (1988).